Homogenization-based design of surface textures in hydrodynamic lubrication

A. Waseem[1], İ. Temizer[1,*,†], J. Kato[2] and K. Terada[3]

[1]*Department of Mechanical Engineering, Bilkent University, 06800 Ankara, Turkey*
[2]*Department of Civil Engineering, Tohoku University, Sendai 980-8579, Japan*
[3]*International Research Institute of Disaster Science, Tohoku University, Sendai 980-8579, Japan*

SUMMARY

An optimization framework is developed for surface texture design in hydrodynamic lubrication. The microscopic model of the lubrication interface is based on the Reynolds equation, and the macroscopic response is characterized through homogenization. The microscale setting assumes a unilateral periodic texture but implicitly accounts for the bilateral motion of the surfaces. The surface texture in a unit cell is described indirectly through the film thickness, which is allowed to vary between prescribed minimum and maximum values according to a morphology variable distribution that is obtained through the filtering of a design variable. The design and morphology variables are discretized using either element-wise constant values or through first-order elements. In addition to sharp textures, which are characterized by pillars and holes that induce sudden transitions between extreme film thickness values, the framework can also attain a variety of non-standard smoothly varying surface textures with a macroscopically isotropic or anisotropic response. Copyright © 2016 John Wiley & Sons, Ltd.

1. INTRODUCTION

Optimality of a design is often assessed both with respect to the macroscopic geometry as well as with respect to the microscopic properties. The optimization of the structural geometry in order to minimize or maximize a macroscopic objective is an area with many continuing challenges and novel applications [1, 2]. Recent topology optimization studies address novel algorithms [3–5] as well as the application of existing robust approaches to multi-material design [6–8], nonlinear behavior [9, 10] and multiphysics scenarios ranging from heat transfer [11, 12] to piezoelectricity [13, 14]. Interface topology can similarly be addressed [15, 16], including contact conditions [17].

The optimization of the constitutive behavior of the structural material as well as of the surfaces or interfaces is a complementary field that is less mature. This problem may be formulated at a phenomenological level through the macroscopic governing equations for the constitutive response. Alternatively, a microscopic problem may be formulated through a direct consideration of the underlying microstructure. Because of the dramatic rise in computational power, such non-phenomenological computational design of materials and surfaces can now be carried out and, with the advent of scalable manufacturing techniques, these designs can be realized [18]. Consequently, there has been a recent surge of interest in designing microstructures that can deliver a desired macroscopic response. Such microstructures can have well-defined constituents as in fiber-reinforced materials [14, 19] or rather flexible topologies with a linear or a nonlinear behavior

---

*Correspondence to: İ. Temizer, Department of Mechanical Engineering, Bilkent University, 06800 Ankara, Turkey
†E-mail: temizer@bilkent.edu.tr

[20–22] as well as entirely random ones [23–25]. In this study, a class of such design problems will be addressed, which are relevant to tribology, namely, the optimal design of surface textures in the context of hydrodynamic lubrication, with homogenization as the core scale-transition method because of its well-established role in topology optimization [26–29].

One of the earliest attempts to optimization in the context of hydrodynamic lubrication is the analysis of Lord Rayleigh [30] toward the determination of an optimal macroscopic surface geometry of a slider bearing in order to maximize its load capacity. A similar analysis was later carried out in [31] where a minimum constraint was placed on the film thickness and a pressure-dependent viscosity was also considered. The slider in a hard disk drive can benefit from similar macroscale optimization approaches, and many studies have focused on this design problem [32–38]. These approaches were also extended to journal bearings [39, 40], with the additional possibility of considering a number of design variables, which include the maximum allowable pressure or fluid film temperature rise [41–44].

In the summarized studies on macroscopic interface geometry design, the core of the optimization algorithm relies on the Reynolds equation, particularly in the case of a focus on load capacity. The Reynolds equation satisfactorily reflects hydrodynamic lubrication effects for a broad range of interface parameters, and its solution delivers the pressure, which allows the interface to carry a normal load [45, 46]. Based on the Reynolds equation, a number of recent studies have directly concentrated on the optimization of the mesoscopic interface geometry by fully or partially endowing the surface typically with pillar-type features that have circular or square cross-sections [47–54]. However, a homogenization-based scheme that concentrates on the microscale through the design of micro-textures with the purpose of attaining a prescribed macroscopic interface response appears not to have been addressed in the literature. This situation is contrary to the case of microstructure design for materials where various studies have been devoted to achieving a desired macroscopic response via a rigorous homogenization-based framework, ranging from specific responses such as a negative Poisson's ratio or a negative thermal expansion coefficient to more general ones that are assessed indirectly through a macroscopic structural objective [55–59]. The development of a similar homogenization-based scheme in the context of hydrodynamic lubrication is the goal of the present study.

The outline of this work is as follows. In Section 2, the homogenization theory for the Reynolds equation is reviewed in a setting that allows for unilateral surface texture with bilateral surface motion. Subsequently, the sensitivity analysis of the macroscopic tensors, which characterize the homogenized response of the textured lubrication interface, is carried out in Section 3. This analysis is carried out in terms of a design variable, which is subjected to discretization and filtering operations toward a morphology variable, which helps formulate the microscale optimization problem in Section 4. Extensive numerical investigations in Section 5 demonstrate the ability of the design framework to capture a variety of textures that may display macroscopically isotropic or anisotropic responses, ranging from sharp ones with holes or pillars to ones that have a smoothly varying surface topography. An outlook toward possible applications and improvements of the developed framework is provided in Section 6.

2. HOMOGENIZATION OF THE REYNOLDS EQUATION

Presently, factors such as partial contact, cavitation, or turbulence will be omitted from the physics of the problem. Instead, attention will be focused to the hydrodynamic lubrication setting where the interface is heterogeneous due to surface roughness. The roughness is assumed to be of the Reynolds type from the outset so that the Reynolds equation may be employed on the microscale in the context of homogenization based on a scale separation assumption [60]. Initially, both of the surfaces will be assigned a roughness in order to summarize homogenization results in the most general setting where either surface could also be moving with a constant velocity [61]. Subsequently, however, only unilateral roughness will be considered although the bilateral motion of the surfaces is intrinsically accounted for. The goal of the present work is to carry out deterministic texture optimization, and hence, periodic textures will be assumed. The problem of constructing a randomly rough surface based on a series of optimal statistical characteristics would also be of interest, although this is outside the scope of this study.

2.1. Two-scale setting

Based on the setting summarized earlier, the heterogeneous (deterministic) Reynolds equation may be expressed with respect to an intermediate flat stationary plane as

$$-\nabla_{\boldsymbol{x}_\varepsilon} \cdot \boldsymbol{q}_\varepsilon(\boldsymbol{x}_\varepsilon, t_\varepsilon) = \frac{\partial h_\varepsilon(\boldsymbol{x}_\varepsilon, t_\varepsilon)}{\partial t_\varepsilon} \tag{2.1}$$

where $\boldsymbol{x}_\varepsilon$ and t_ε are the absolute position and time. The interface fluid flux $\boldsymbol{q}_\varepsilon(\boldsymbol{x}_\varepsilon, t_\varepsilon)$ depends on the fluid film thickness $h_\varepsilon(\boldsymbol{x}_\varepsilon, t_\varepsilon)$ and the generated pressure $p_\varepsilon(\boldsymbol{x}_\varepsilon, t_\varepsilon)$ via

$$\boldsymbol{q}_\varepsilon = -\frac{h_\varepsilon^3}{12\mu} \boldsymbol{g}_\varepsilon + \frac{h_\varepsilon}{2} \boldsymbol{U} \tag{2.2}$$

where μ is the fluid viscosity, $\boldsymbol{g}_\varepsilon = \nabla_{\boldsymbol{x}_\varepsilon} p_\varepsilon$ is the pressure gradient, and $\boldsymbol{U} = \boldsymbol{U}^+ + \boldsymbol{U}^-$, with $\boldsymbol{U}^+$ as the velocity of the upper surface and $\boldsymbol{U}^-$ as that of the lower one.

$\varepsilon \ll 1$ is a scale factor that is proportional to the roughness wavelength and indicates highly oscillatory quantities. For homogenization purposes, it may be employed to invoke the two-scale expressions

$$\boldsymbol{x}_\varepsilon = \boldsymbol{x} + \varepsilon \boldsymbol{y} \quad , \quad t_\varepsilon = t + \varepsilon \tau \tag{2.3}$$

where $\boldsymbol{x}$ and t are the coarse scale (macroscopic) position and time while $\boldsymbol{y}$ and τ are their independent fine scale (microscopic) counterparts. The film thickness is then assigned the form

$$h_\varepsilon(\boldsymbol{x}_\varepsilon, t_\varepsilon) = h(\boldsymbol{x}, t, \boldsymbol{y}, \tau) = h_0(\boldsymbol{x}, t) + h^+(\boldsymbol{y} - \boldsymbol{U}^+\tau) - h^-(\boldsymbol{y} - \boldsymbol{U}^-\tau) \tag{2.4}$$

where h_0 describes the smooth macroscopic variation of the film thickness while $h^\pm$ are the roughness contributions with zero mean from the upper and lower surfaces.

The solution of the Reynolds equation on a macroscopic domain, subject to appropriate boundary conditions on the pressure or the normal components of the flux, is standard yet significantly costly for small ε. This cost is alleviated through homogenization.

2.2. Asymptotic homogenization

Briefly summarizing for the purposes of this work, following [61] and the discussions in [62], the classical homogenization procedure is now carried out by substituting (2.2)–(2.4) into (2.1) together with the asymptotic expansion

$$p_\varepsilon(\boldsymbol{x}_\varepsilon, t_\varepsilon) = p_0(\boldsymbol{x}, t, \boldsymbol{y}, \tau) + \varepsilon p_1(\boldsymbol{x}, t, \boldsymbol{y}, \tau) + \varepsilon^2 p_2(\boldsymbol{x}, t, \boldsymbol{y}, \tau) + \mathcal{O}(\varepsilon^3) \tag{2.5}$$

and finally invoking scale separation via $\varepsilon \to 0$. Gathering terms of equal powers of ε, one concludes from the ε^{-2}-terms that $p_0 = p_0(\boldsymbol{x}, t, \tau)$, that is, there is no $\boldsymbol{y}$-dependence of p_0. Upon linearly expanding p_1 in terms of the macroscopic pressure gradient $\boldsymbol{G}(\boldsymbol{x}, t, \tau) = \nabla_{\boldsymbol{x}} p_0$ and the relative velocity $\boldsymbol{V} = \boldsymbol{U}^+ - \boldsymbol{U}^-$ via

$$p_1 = \boldsymbol{G} \cdot \boldsymbol{\omega} - \boldsymbol{V} \cdot \boldsymbol{\Omega} \quad , \tag{2.6}$$

the ε^{-1}-terms deliver homogenized coefficient tensors $\boldsymbol{A}(\boldsymbol{x}, t, \tau)$ and $\boldsymbol{B}(\boldsymbol{x}, t, \tau)$ in terms of $\boldsymbol{\omega}(\boldsymbol{x}, t, \boldsymbol{y}, \tau)$ and $\boldsymbol{\Omega}(\boldsymbol{x}, t, \boldsymbol{y}, \tau)$ (Section 2.3) with which the homogenized Reynolds equation that is obtained from the ε^0-terms may be expressed as

$$-\nabla_{\boldsymbol{x}} \cdot \boldsymbol{Q} = \frac{\partial h_0}{\partial t} \tag{2.7}$$

where the macroscopic fluid flux $\boldsymbol{Q}(\boldsymbol{x}, t, \tau)$ has the form

$$Q = -AG + \frac{h_0}{2}U + BV \quad . \tag{2.8}$$

Here, the first term is the Poiseuille contribution, and the sum of the remaining terms

$$b = \frac{h_0}{2}U + BV \tag{2.9}$$

is the Couette contribution.

These results are consistent with classical averaging-based approaches. If the domain of a periodic unit cell is $\mathcal{Y}$, which evolves with a period $\mathcal{T}$ due to surface motion, and averaging over this domain is denoted by $\langle \cdot \rangle = \frac{1}{|\mathcal{Y}|} \int_{\mathcal{Y}} \cdot \, \mathrm{da}$, one obtains the relations

$$h_0 = \langle h \rangle \quad , \quad G = \langle g \rangle \quad , \quad Q = \langle q \rangle \tag{2.10}$$

where the microscopic gradient g and flux q are defined by

$$g = G + \nabla_y p_1 \quad , \quad q = -\frac{h^3}{12\mu}g + \frac{h}{2}U \quad . \tag{2.11}$$

2.3. Cell problems and unilateral roughness

The tensors A and B in (2.8) are defined through

$$A_{ij} = \left\langle \frac{h^3}{12\mu}\left(\delta_{ij} + \lambda_i^j\right)\right\rangle \quad , \quad B_{ij} = \left\langle \frac{h^3}{12\mu}\Lambda_i^j\right\rangle \tag{2.12}$$

where δ_{ij}, the Kronecker delta, refers to the components of the identity tensor I and

$$\lambda_i^j = \frac{\partial \omega_j}{\partial y_i} \quad , \quad \Lambda_i^j = \frac{\partial \Omega_j}{\partial y_i} \quad . \tag{2.13}$$

Here, the $\mathcal{Y}$-periodic and $\mathcal{T}$-periodic vectors ω and Ω satisfy, subject to periodic boundary conditions,

$$\frac{\partial}{\partial y_i}\left(\frac{h^3}{12\mu}\lambda_i^j\right) = -\frac{\partial}{\partial y_j}\left(\frac{h^3}{12\mu}\right) \quad , \quad \frac{\partial}{\partial y_i}\left(\frac{h^3}{12\mu}\Lambda_i^j\right) = \frac{\partial}{\partial y_j}\left(\frac{h^+ + h^-}{2}\right) \quad . \tag{2.14}$$

Because of the tangential motion of the surfaces, the values of h^+ and h^- in (2.4) continuously change at a fixed point in the interface, which leads to rapid oscillations in the coefficients of the differential equations and therefore to rapid oscillations of A and B, and hence of p_0, in τ. When both surfaces are periodically rough with a commensurate frequency, one obtains the *unsteady* hydrodynamic lubrication regime where these oscillations are of finite magnitude even at scale separation and must be resolved for an accurate macroscopic response prediction. When only one surface is rough, however, the oscillations disappear so that all macroscopic quantities remain dependent only on x and t. This is the setting that will be addressed in the present study. However, both of the surfaces may be moving in general. If the rough surface is stationary, then the microscopic quantities oscillate in space only and this regime is referred to as *stationary*. If the rough surface also moves, then the microscopic oscillations are in space and time, which is referred to as the *quasi-stationary* regime. The employed framework addresses both of these regimes.

Consider the special case of a periodic cell where the lower surface ($\mathcal{S}^-$) is stationary and rough with $h^- = \overline{h}(y)$ and the upper surface ($\mathcal{S}^+$) is flat and moving with a velocity $U^+ = \overline{U}$. Let the cell problems (2.14) deliver for this case the homogenized coefficient tensors $A = \overline{A}$ and $B = \overline{B}$. Because $V = \overline{U}$, (2.9) delivers $b = \left(h_0/2\,I + \overline{B}\right)\overline{U}$, or $b = C\overline{U}$ where $C = h_0/2\,I + \overline{B}$.
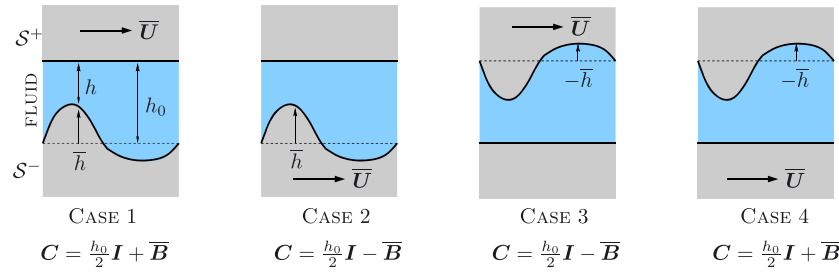
Figure 1. Four different cases regarding the stationary and quasi-stationary regimes are depicted on a periodic cell. The roughness is switched from $\mathcal{S}^-$ to $\mathcal{S}^+$ by taking a mirror image with respect to an intermediate plane. All the cases share the same $A = \overline{A}$ and $U = \overline{U}$ as well as the same $h = h_0 - \overline{h}$ distribution while, depending on the particular case, $V = \pm \overline{U}$ and $B = \pm \overline{B}$ where $B = \overline{B}$ corresponds to CASE 1. For all cases, (2.9) simplifies to $b = C\overline{U}$.

This setup is one of the four different cases (CASE 1) regarding the stationary and quasi-stationary regimes as depicted in Figure 1 where either h^- or $-h^+$ equals $\overline{h}$ and either U^- or U^+ equals $\overline{U}$. Because of the structure of the cell problems (2.14), it is immediately observed that all of these cases share the same $A = \overline{A}$ because the $h = h_0 - \overline{h}$ distribution is the same in all cases. Moreover, one can readily show that it is always possible to employ the expression $b = C\overline{U}$ where $C = h_0/2\, I \pm \overline{B}$ where the sign depends on the side of roughness and motion. Hence, the special case considered covers the remaining three cases through the knowledge of $\overline{A}$ and $\overline{B}$. Similarly, the case of bilateral surface motion is also covered (see Appendix A for a discussion). Consequently, an optimization procedure for the specialized setup of CASE 1 entirely addresses all other cases where, additionally, both surfaces could be moving.

In view of the preceding discussion, the special case with a stationary and rough lower surface combined with a flat upper surface moving at a velocity $U^+ = V = U$ is considered in all subsequent analysis, and optimization is carried out in terms of A and C. For this purpose, using $h_0 = \langle h \rangle$, it is useful to explicitly express C as

$$C_{ij} = \left\langle \frac{h}{2}\delta_{ij} + \frac{h^3}{12\mu}\Lambda_i^{\,j} \right\rangle \tag{2.15}$$

where $\Lambda_i^{\,j}$ satisfies

$$\frac{\partial}{\partial y_i}\left(\frac{h^3}{12\mu}\Lambda_i^{\,j} \right) = -\frac{\partial}{\partial y_j}\left(\frac{h}{2} \right) \quad , \tag{2.16}$$

leading to the specialized macroscopic flux expression

$$Q = -A\,G + C\,U \quad . \tag{2.17}$$

3. SENSITIVITY ANALYSIS

At the periodic cell level, the film thickness $h(\rho) = h_0 - \overline{h}(\rho)$ will be controlled by a finite number of degrees of freedom s^I (to be specified), which allow tuning the texture of the rough surface. In order to design the texture toward a desired macroscopic response, it is necessary to evaluate the sensitivities of A and C with respect to s^I. The sensitivities of A and $b = C\overline{U}$ for their Taylor expansion around given local values with respect to a generic variable have been discussed in [63]. Presently, the sensitivity analysis is first carried out explicitly with respect to s^I for A, and subsequently a similar approach is employed toward the sensitivity of C. As in [63], a direct method is adopted for the sensitivity analysis, versus the adjoint method [1]. For a slightly more compact notation, the definitions

$$a = \frac{h^3}{12\mu} \quad , \quad b = \frac{h}{2} \tag{3.1}$$

will be employed. A validation of the derived analytical sensitivities will be carried out within the numerical investigations.

3.1. Poiseuille term

The sensitivity of A follows from (2.12):

$$\frac{\partial A_{ij}}{\partial s^I} = \left\langle \frac{\partial a}{\partial s^I} \left(\delta_{ij} + \lambda_i^j \right) + a \frac{\partial \lambda_i^j}{\partial s^I} \right\rangle \quad . \tag{3.2}$$

In order to calculate $\frac{\partial \lambda_i^j}{\partial s^I}$, let ϕ be a periodic test function. The strong form of the cell problem (2.14) for λ_k^i may be expressed in weak form as

$$\left\langle a \lambda_k^i \frac{\partial \phi}{\partial y_k} \right\rangle = -\left\langle a \frac{\partial \phi}{\partial y_i} \right\rangle, \tag{3.3}$$

and if $\phi = \frac{\partial \omega^j}{\partial s^I}$ is chosen, then one obtains an expression involving the target sensitivity:

$$\left\langle a \frac{\partial \lambda_i^j}{\partial s^I} \right\rangle = -\left\langle a \lambda_k^i \frac{\partial \lambda_k^j}{\partial s^I} \right\rangle \quad . \tag{3.4}$$

To identify the right-hand side, note that the sensitivity of the cell problem (2.14) for λ_k^j with respect to s^I yields

$$\frac{\partial}{\partial y_k} \left(\frac{\partial a}{\partial s^I} \lambda_k^j + a \frac{\partial \lambda_k^j}{\partial s^I} \right) = -\frac{\partial}{\partial y_j} \left(\frac{\partial a}{\partial s^I} \right), \tag{3.5}$$

which may be expressed in weak form, using a periodic test function π, as

$$\left\langle \frac{\partial a}{\partial s^I} \lambda_k^j \frac{\partial \pi}{\partial y_k} + a \frac{\partial \lambda_k^j}{\partial s^I} \frac{\partial \pi}{\partial y_k} \right\rangle = -\left\langle \frac{\partial a}{\partial s^I} \frac{\partial \pi}{\partial y_j} \right\rangle \tag{3.6}$$

and if $\pi = \omega^i$ is chosen then one obtains an expression for the right-hand side of (3.4):

$$-\left\langle a \lambda_k^i \frac{\partial \lambda_k^j}{\partial s^I} \right\rangle = \left\langle \frac{\partial a}{\partial s^I} \lambda_k^j \lambda_k^i + \frac{\partial a}{\partial s^I} \lambda_j^i \right\rangle \quad . \tag{3.7}$$

Making use of this result in (3.2) via (3.4) and rearranging, one finally obtains

$$\frac{\partial A_{ij}}{\partial s^I} = \left\langle \frac{\partial a}{\partial s^I} \left(\delta_{ik} + \lambda_k^i \right) \left(\delta_{jk} + \lambda_k^j \right) \right\rangle \quad . \tag{3.8}$$

This result is expected in view of the results for homogenization-based sensitivity analysis in the context of linear elasticity and linear thermal conduction [1] but has been re-derived here in the context of hydrodynamic lubrication for completeness and as a means of building a foundation for the sensitivity analysis of the non-standard accompanying term C. In this context, it is useful to note an alternative form of A that establishes a clear link to (3.8), which may easily be derived by switching the free index i in (3.3) to j, choosing $\phi = \omega^i$ and adding the resulting expression to the definition (2.12) of A:

$$A_{ij} = \left\langle a \left(\delta_{ik} + \lambda_k^i \right) \left(\delta_{jk} + \lambda_k^j \right) \right\rangle \quad . \tag{3.9}$$

3.2. Couette term

The sensitivity of $\boldsymbol{C}$ follows from (2.15)

$$\frac{\partial C_{ij}}{\partial s^I} = \left\langle \frac{\partial b}{\partial s^I} \delta_{ij} + \frac{\partial a}{\partial s^I} \Lambda_i^j + a \frac{\partial \Lambda_i^j}{\partial s^I} \right\rangle \tag{3.10}$$

wherein the last term $\frac{\partial \Lambda_i^j}{\partial s^I}$ must be calculated. Note that, upon choosing $\phi = \frac{\partial \Omega^j}{\partial s^I}$ and rearranging, the weak form (3.3) delivers an expression involving this sensitivity:

$$\left\langle a \frac{\partial \Lambda_i^j}{\partial s^I} \right\rangle = - \left\langle a \lambda_k^i \frac{\partial \Lambda_k^j}{\partial s^I} \right\rangle \quad . \tag{3.11}$$

The identification of the right-hand side requires the sensitivity of the cell problem (2.16) for Λ_k^i:

$$\frac{\partial}{\partial y_k} \left(\frac{\partial a}{\partial s^I} \Lambda_k^j + a \frac{\partial \Lambda_k^j}{\partial s^I} \right) = - \frac{\partial}{\partial y_j} \left(\frac{\partial b}{\partial s^I} \right) \quad . \tag{3.12}$$

Using a periodic test function π, one may express its weak form as

$$\left\langle \frac{\partial \pi}{\partial y_k} \frac{\partial a}{\partial s^I} \Lambda_k^j + \frac{\partial \pi}{\partial y_k} a \frac{\partial \Lambda_k^j}{\partial s^I} \right\rangle = - \left\langle \frac{\partial \pi}{\partial y_j} \frac{\partial b}{\partial s^I} \right\rangle \tag{3.13}$$

that delivers, upon choosing $\pi = \omega^i$ and rearranging, an expression for the right-hand side of (3.11):

$$- \left\langle a \lambda_k^i \frac{\partial \Lambda_k^j}{\partial s^I} \right\rangle = \left\langle \lambda_k^i \frac{\partial a}{\partial s^I} \Lambda_k^j + \lambda_j^i \frac{\partial b}{\partial s^I} \right\rangle. \tag{3.14}$$

Making use of this result in (3.10) via (3.11) and rearranging, one finally obtains a mixed expression involving the cell problem solutions for both $\boldsymbol{\omega}$ and $\boldsymbol{\Omega}$:

$$\frac{\partial C_{ij}}{\partial s^I} = \left\langle \frac{\partial b}{\partial s^I} \left(\delta_{ij} + \lambda_j^i \right) + \frac{\partial a}{\partial s^I} \left(\Lambda_i^j + \lambda_k^i \Lambda_k^j \right) \right\rangle \quad . \tag{3.15}$$

Similar to (3.9), an alternative expression for $\boldsymbol{C}$ that establishes a clear link to (3.15) may be derived by expressing (2.16) in weak form through a periodic test function ϕ, making the special choice $\phi = \omega^i$ and subsequently adding the resulting expression to the definition (2.15) of $\boldsymbol{C}$:

$$C_{ij} = \left\langle b \left(\delta_{ij} + \lambda_j^i \right) + a \left(\Lambda_i^j + \lambda_k^i \Lambda_k^j \right) \right\rangle \quad . \tag{3.16}$$

4. TEXTURE DESIGN

4.1. Design variables

The design variables $s^I \in [0, 1]$ are the primary degrees of freedom in the optimization algorithm, which discretize the *design* variable $s \in [0, 1]$ through shape functions N^I:

$$s = \sum_I N^I s^I \tag{4.1}$$

In this work, the shape functions will be chosen either in the classical discrete fashion as element-wise constant ($S0$) [1] or through a continuous piecewise linear approximation ($S1$) [64]. The homogenization variables ω and Ω will be discretized by linear ($Q1$) elements, thereby leading to two element possibilities for texture optimization: $Q1S0$ or $Q1S1$.

The variable s is usually employed within the texture description after an intermediate filtering stage. The filtering operation will be denoted by $\mathcal{F}$, which delivers the degrees of freedom $\rho^K \in [0, 1]$ of the *morphology* variable $\rho \in [0, 1]$ that inherits the discretization of s. Specifically, the *morphology filter* $\mathcal{F}$ operates on the degrees of freedom of s within a neighborhood $\mathcal{D}^K$ to deliver the degree of freedom ρ^K of the filtered morphology variable ρ:

$$\rho = \sum_K N^K \rho^K = \sum_K N^K \mathcal{F}\left(\mathcal{D}^K, s\right) \quad . \tag{4.2}$$

Different filters that have recently been proposed in [65] will be employed in this work, as summarized in Table I (see also [66, 67]). In these filters, the weights $w^{KI} \in [0, 1]$ ensure that ρ^K remain within $[0, 1]$. The weights may be suitably chosen constants or of the conic type, which decrease with an increasing distance from the degree of freedom I. Here, the latter type will be employed because they were observed to perform better in texture optimization. To define conic weights, let $\mathcal{D}^K$ be defined as the set of nodes I whose distance $d(K, I)$ to node K are less than or equal to a radius R. The conic weights have the form

$$w^{KI} = \begin{cases} \frac{R - d(K,I)}{\sum_{J \in \mathcal{D}^J} R - d(K,J)} & I \in \mathcal{D}^K \\ 0 & I \neq \mathcal{D}^K \end{cases} \tag{4.3}$$

so that $\sum_I w^{KI} = 1$.

It is remarked that the morphology filters operate on the design variables and, hence, directly influence the sensitivities. A well-established alternative approach is to filter the sensitivities only. Although it will not be employed explicitly, it is noted that this *sensitivity filter* can be formulated as a special case of the geometric erode filter using $\alpha = 0$, but re-assigning $\rho^I = s^I$ to leave the design variables unchanged [65].

Table I. Different filters $\mathcal{F}$ are expressed, which operate in a neighborhood $\mathcal{D}^K$. Here, $w^{KI} \in [0, 1]$ are the conic weights, and α is a control parameter that is chosen as 10^{-3} for harmonic-type and geometric-type filters and as 100 for the exponential-type filter.

Method	Filter $\rho^K = \mathcal{F}\left(\mathcal{D}^K, s\right)$	Sensitivity $\frac{\partial \rho^K}{\partial s^I}$
Linear	$\rho^K = \sum_I w^{KI} s^I$	w^{KI}
Harmonic erode	$\frac{1}{\rho^K + \alpha} = \sum_I \frac{w^{KI}}{s^I + \alpha}$	$w^{KI} \frac{(\rho^K + \alpha)^2}{(s^I + \alpha)^2}$
Harmonic dilate	$\frac{1}{1 - \rho^K + \alpha} = \sum_I \frac{w^{KI}}{1 - s^I + \alpha}$	$w^{KI} \frac{(1 - \rho^K + \alpha)^2}{(1 - s^I + \alpha)^2}$
Geometric erode	$\ln(\rho^K + \alpha) = \sum_I w^{KI} \ln(s^I + \alpha)$	$w^{KI} \frac{(\rho^K + \alpha)}{(s^I + \alpha)}$
Geometric dilate	$\ln(1 - \rho^K + \alpha) = \sum_I w^{KI} \ln(1 - s^I + \alpha)$	$w^{KI} \frac{(1 - \rho^K + \alpha)}{(1 - s^I + \alpha)}$
Exponential erode	$e^{\alpha(1 - \rho^K)} = \sum_I w^{KI} e^{\alpha(1 - s^I)}$	$w^{KI} \frac{e^{\alpha(1 - s^I)}}{e^{\alpha(1 - \rho^K)}}$
Exponential dilate	$e^{\alpha \rho^K} = \sum_I w^{KI} e^{\alpha s^I}$	$w^{KI} \frac{e^{\alpha s^I}}{e^{\alpha \rho^K}}$

4.2. Texture description

Using ρ, the surface texture is indirectly expressed through the film thickness

$$h(\rho) = h_{\min} + (h_{\max} - h_{\min})\rho^\eta \quad \in [h_{\min}, h_{\max}] \tag{4.4}$$

where $h_{\min}$ and $h_{\max}$ are the desired minimum and maximum film thickness values and $\eta \geqslant 1$ is a parameter that determines whether the goal texture has relatively sharp transitions between $h_{\min}$ and $h_{\max}$, corresponding to $\eta > 1$ (for instance, $\eta = 3$) and referred to as a 0-OR-1 design that is characterized by pillars and holes on a surface, or smooth transitions (ideally $\eta = 1$) that deliver a 0-TO-1 design that is characterized by bumps and dimples. The design must additionally satisfy a desired macroscopic film thickness

$$\langle h \rangle = h_0 \quad \longrightarrow \quad \langle \rho^\eta \rangle = \frac{h_0 - h_{\min}}{h_{\max} - h_{\min}} \quad . \tag{4.5}$$

Based on the texture description, the calculation of the sensitivities (3.8) and (3.15) is indirectly addressed through a generic form $\left\langle \frac{\partial \mathcal{H}(h)}{\partial s^I} \right\rangle$ where $\mathcal{H}$ is an arbitrary function of h [64]:

$$\left\langle \frac{\partial \mathcal{H}(h)}{\partial s^I} \right\rangle = \left\langle \frac{\partial \mathcal{H}}{\partial h} \frac{\partial h}{\partial \rho} \sum_K \frac{\partial \rho}{\partial \rho^K} \frac{\partial \rho^K}{\partial s^I} \right\rangle = \left\langle \frac{\partial \mathcal{H}}{\partial h} \left\{ \eta(h_{\max} - h_{\min})\rho^{\eta-1} \right\} \sum_K N^K \frac{\partial \rho^K}{\partial s^I} \right\rangle$$

$$= \frac{1}{|\mathcal{Y}|} \sum_K \int_{\mathcal{Y}^K} \left(\frac{\partial \mathcal{H}}{\partial h} \left\{ \eta(h_{\max} - h_{\min})\rho^{\eta-1} \right\} N^K \frac{\partial \rho^K}{\partial s^I} \right) \mathrm{d}a \quad . \tag{4.6}$$

Here, $\mathcal{Y}^K \subset \mathcal{Y}$ indicates the span of N^K. When ρ is element-wise constant, K indexes the elements and $N^K = 1$ only within the domain of its element.

4.3. Optimization

For the formulation of the optimization problem, the objective function

$$\varphi(s) = \frac{1}{2} \left(\frac{\|A - A^*\|^2}{\|A^*\|^2} + \frac{\|C - C^*\|^2}{\|C^*\|^2} \right) \tag{4.7}$$

is introduced where $\|\cdot\|$ denotes the Frobenius norm and $\{A^*, C^*\}$ are the *target* values of the homogenized coefficient tensors $\{A, C\}$. Additionally, a constraint function

$$\chi(s) = \frac{(\langle h \rangle - h_0)^2}{h_0^2} \tag{4.8}$$

is introduced in order to eventually ensure, via (4.5), that the mean film thickness is satisfied by the design, which essentially plays the role of the volume fraction constraint in topology optimization. Also recalling that the design variables s^I are constrained to the interval $[0, 1]$, the optimization problem is formulated as

$$\textit{minimize } \varphi(s), \textit{ subject to } \chi(s) = 0 \textit{ and } s \in [0, 1] \quad . \tag{4.9}$$

For a particular lubrication interface geometry with prescribed boundary conditions, the pressure variation across the interface is entirely determined by the distributions of $\{A, C\}$. The ability to tune the pressure variation is of prime importance in lubrication because it directly controls global performance criteria such as the load capacity of the interface. Therefore, in the context of surface engineering, one may attempt to determine optimal $\{A, C\}$ distributions in the first step of a design problem in order to obtain a pressure variation that satisfies desired global performance criteria. This optimization task does not necessarily require a homogenization-based framework. However, if these optimal distributions are denoted by $\{A^*, C^*\}$, the second step would be to determine the

texture that delivers the corresponding target values $\{A^*, C^*\}$ at each point across the interface where the gap h_0 between the interacting surfaces is known. The optimization problem stated in (4.9) serves to test precisely this ability of the developed homogenization-based design framework. A more advanced design setting would discard the need to determine an optimal $\{A, C\}$ distribution in a first step and would instead directly link the global performance criteria on the macroscale to the texture geometry on the microscale, thereby also allowing microscopic design criteria such as manufacturing constraints to be taken into account simultaneously with the macroscopic objectives and constraints. Such a two-scale design setting, however, requires meeting additional challenges that are outside the scope of the present study (see also Section 6).

In this work, the *method of moving asymptotes (MMA)* will be employed as the optimization algorithm in view of its proven success [68]. MMA operates based on the values as well as the sensitivities of the objective function and the equality constraint in order to reach a minimum that satisfies the inequality constraints. The sensitivities $\frac{\partial \varphi}{\partial s^I}$ and $\frac{\partial \chi}{\partial s^I}$ for this purpose are computed via the analysis of Section 3 together with the general expression (4.6).

5. NUMERICAL INVESTIGATIONS

5.1. Target textures

Within the tests for texture design, a series of benchmark target textures of the 0-OR-1 and 0-TO-1 type will first be described on a given mesh resolution and an element type ($Q1S0$ or $Q1S1$). Each texture may deliver a macroscopically isotropic or anisotropic response. The macroscopic quantities $\{A^*, C^*, h_0\}$ associated with a target texture will then be fed into the MMA algorithm as input values that will drive the optimization procedure toward a design output. Employing target textures to generate the input set will (i) allow for a visual assessment of the optimization results, in particular by indicating if it is possible to obtain identical macroscopic responses from significantly different textures, and also (ii) help circumventing a laborious trial and error stage in order to ensure that the prescribed target macroscopic quantities are actually physically attainable by a texture (cf. Section 5.4). In all cases, the minimum and maximum film thicknesses in (4.4) are set to $h^- = 0.1\ \mu$m and $h^+ = 3\ \mu$m while $\eta = 3$ is employed for 0-OR-1 design and $\eta = 1$ is employed for 0-TO-1 design. The viscosity of the fluid is set to $\mu = 0.14$ Pa·s. The effect of the viscosity is not independently investigated because, via (2.12) and (2.14), one may observe that C is independent of the viscosity while A is inversely proportional to it.

On a given mesh resolution, the textures will be visualized as depicted in Figure 2. The Reynolds equation that constitutes the basis for the homogenization scheme is a 2D formulation that operates on a periodic unit cell, which may be tiled to generate a surface where the pattern appears more clearly. For further clarity, 3D visualizations will additionally be presented. In order to distinguish 0-OR-1 and 0-TO-1 textures, different coloring schemes will be employed to indicate the height variation across the rough surface from a minimum value (which corresponds to maximum film thickness $h = h^+$) to a maximum value (which corresponds to a minimum film thickness $h = h^-$). The target macroscopic response $\{A^*, C^*, h_0\}$ and the corresponding homogeneous response for each case are summarized in Appendix B.

5.2. Default numerical choices

In order to enable the reproducibility of the presented results, it is noted that the default MMA parameters [69] were preserved, except for the move limit parameter (`move` in `mmasub.m`), which was reduced from its default value of 1 to 0.1 because a highly oscillatory optimization process was often observed otherwise. Convergence was declared when φ decreased below a tolerance of $\text{TOL}_\varphi = 10^{-3}$ and χ decreased below $\text{TOL}_\chi = 10^{-4}$. The tolerance on the constraint is typically very quickly satisfied during optimization iterations, that is, most of the numerical cost is due to the low tolerance on the objective function. During implementation, in order to obtain a better convergence performance, φ was scaled to $\varphi' = 100\varphi + 1$, which roughly picks values in the interval $[1, 100]$ with a corresponding convergence tolerance $\text{TOL}_{\varphi'} = 1.1$. For completeness, the number of iterations to convergence will be reported for each case.

(a-1) 0-OR-1: 2D tiled   (a-2) 2D unit cell   (a-3) 3D unit cell   (a-4) 0-OR-1: 3D tiled

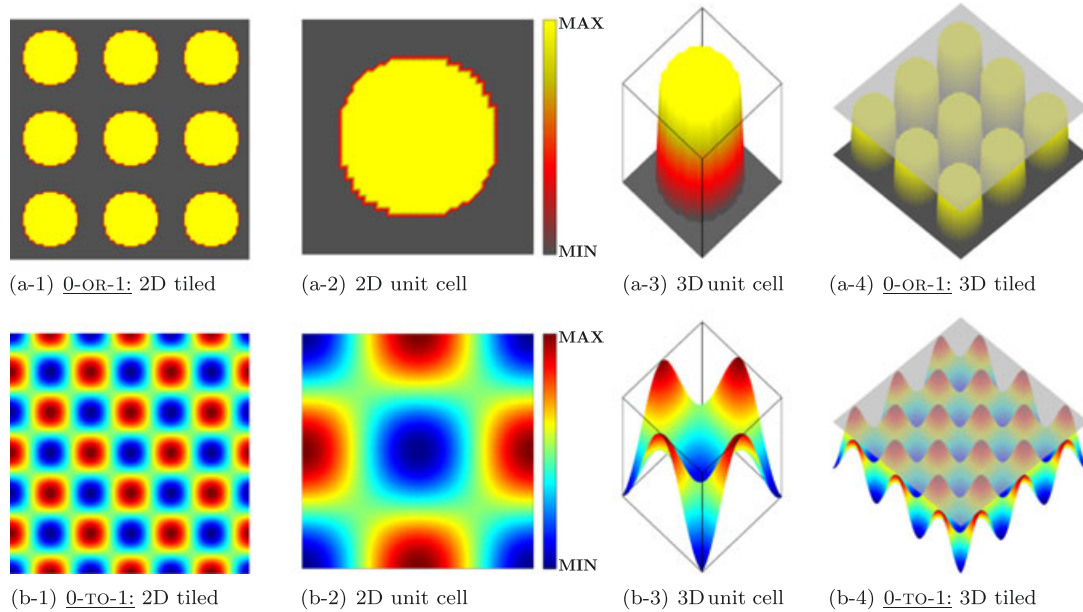(b-1) 0-TO-1: 2D tiled   (b-2) 2D unit cell   (b-3) 3D unit cell   (b-4) 0-TO-1: 3D tiled

Figure 2. 2D unit cells for 0-OR-1 and 0-TO-1 designs are depicted together with their corresponding periodic tilings as well as 3D visualizations. The light gray surface indicates the moving upper surface and the coloring scheme, individual to the type of the design, encodes the height across the stationary lower surface. Consequently, MAX is where the film thickness is a minimum while MIN is where it is a maximum.

The unit cell $\mathcal{Y}$ of periodicity will be modeled as a square with an edge length of $L = 10\ \mu m$ and discretized with a mesh of $N \times N$ elements, with $Q1S1$ as the default element type. However, the absolute edge length only affects the frequency of oscillations in the macroscopic response for bilateral roughness and is irrelevant to homogenization results for the present case of unilateral roughness. Consequently, during implementation, the distance and the radius for the calculation of the weights in (4.3) for filtering purposes will be measured in terms of element or node index coordinates (X, Y). In the case of element-wise constant design variables (i.e., $Q1S0$ element), the element indices are employed. These lie in the interval $[1, N]$, and the distance of element K to I is measured by $d(K, I) = \sqrt{(X_K - X_I)^2 + (Y_K - Y_I)^2}$. The same holds in the case of a continuous piecewise linear design variable (i.e., $Q1S1$ element) where the node indices are employed instead. Note that, although the node index ranges from 1 to $N + 1$, the nodes which lie on periodically linked opposing edges are not independent such that the number of independent nodes along an edge is also N. For all the cases tested in this work, the results were observed to rapidly settle on a pattern with increasing mesh resolution, indicating that a resolution of $N = 40$ can be satisfactorily employed. Note that the filter radius must be scaled in order to preserve the feature size if the mesh resolution is modified.

Filtering delivers results that are closer to the target textures and will be employed in the default setting. The feature size in the designed texture is controlled by the ratio R/N, and filtering is applied periodically. The default filter radius $R \geqslant 1$ is equal to $N/10 = 4$. For 0-OR-1 design, the exponential erode filter from Table I will be selected because it generates sharp transitions and leads to faster convergence among other filters of the erode/dilate type for the cases tested in this work. The linear filter naturally attempts to achieve smooth transitions and hence is selected for 0-TO-1 design. It is remarked that filtering will be applied without modification of the filter parameters until convergence, although gradually turning it off during the iterations may be beneficial for 0-OR-1 design [57].

Based on the default numerical parameter choices, target inputs are depicted together with the output designs in Figure 3 for 0-OR-1 textures with a macroscopically isotropic response and in Figure 4 for anisotropic ones. Similarly, Figures 5 and 6 summarize the results for macroscopically isotropic and anisotropic 0-TO-1 textures. In most cases, convergence has been achieved in less
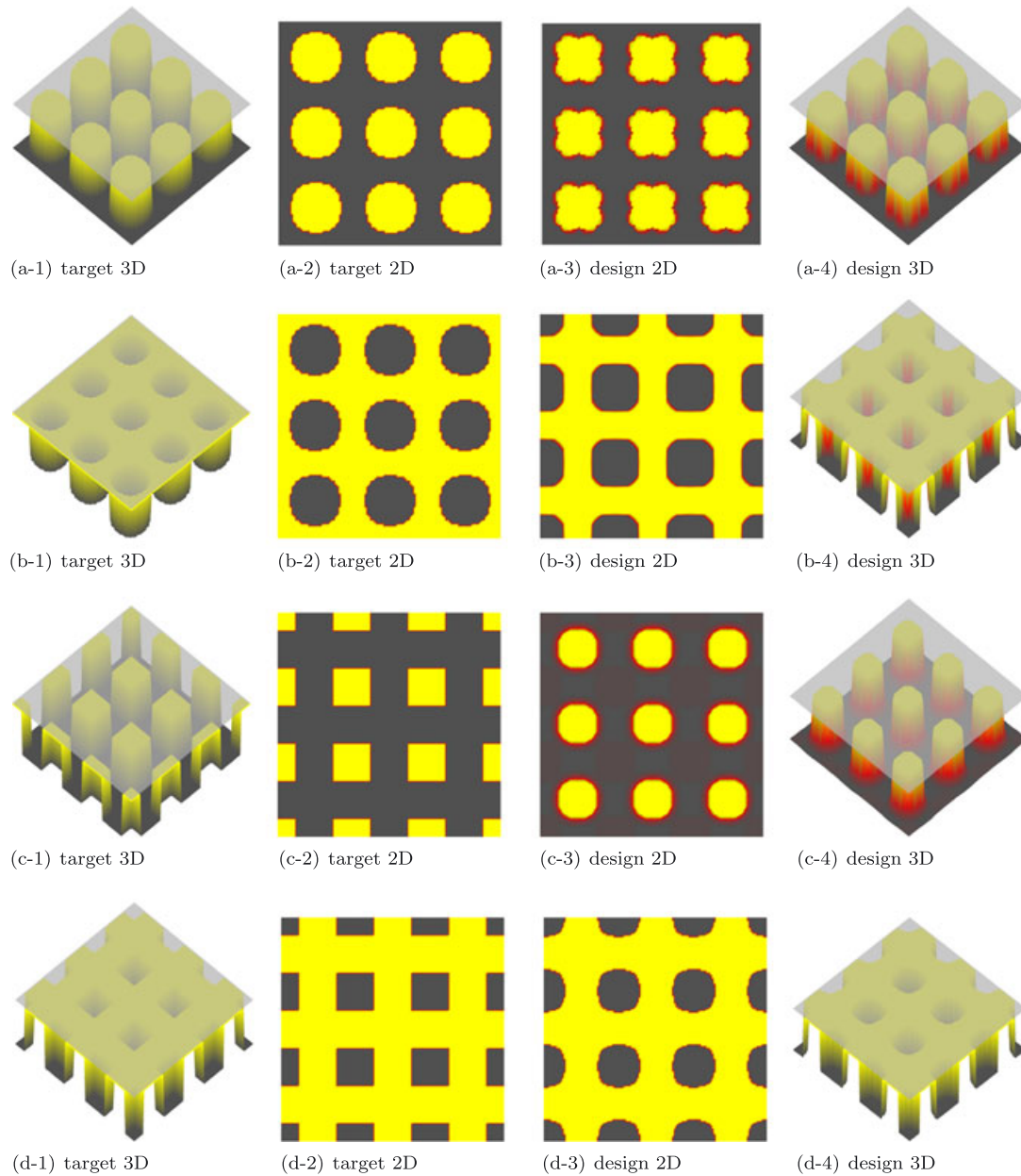
(a-1) target 3D   (a-2) target 2D   (a-3) design 2D   (a-4) design 3D

(b-1) target 3D   (b-2) target 2D   (b-3) design 2D   (b-4) design 3D

(c-1) target 3D   (c-2) target 2D   (c-3) design 2D   (c-4) design 3D

(d-1) target 3D   (d-2) target 2D   (d-3) design 2D   (d-4) design 3D

Figure 3. Benchmark target textures of the 0-OR-1 type displaying a macroscopically *isotropic* response are depicted together with the output designs from the optimization algorithm based on the default numerical choices. The number of iterations to convergence were (a) 93 for the circular pillar texture, (b) 47 for the circular hole texture, (c) 82 for the square pillar texture, and (d) 93 for the square hole texture. See Table A.1 in Appendix B for corresponding target responses.

than 100 iterations, and the output designs compare favorably with the target textures, demonstrating the ability of the framework to capture a broad range of isotropic and anisotropic macroscopic responses, which include sharp textures with pillars and holes as well as smooth textures with dimples and bumps. It is noted that although the major goal of a 0-OR-1 design is to achieve extreme values of h, the ellipsoidal texture in Figure 4 also indicates the ability of this setup to capture sharp features with respect to an intermediate plane.

It is remarked that in the default setting the algorithm has been initiated with a uniform s-distribution at a value s_0 such that $h = h_0$ but by additionally perturbing the value of s with index
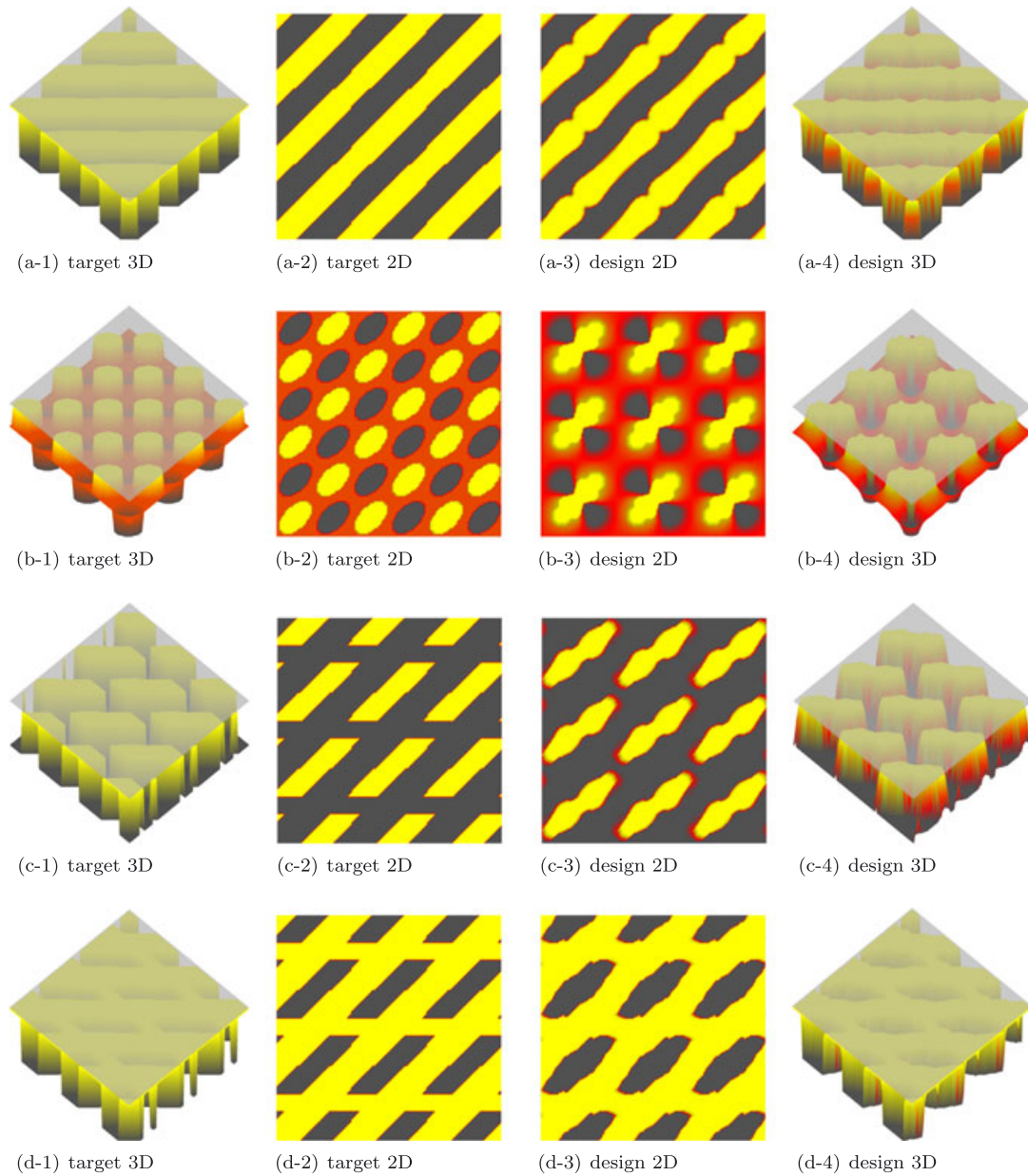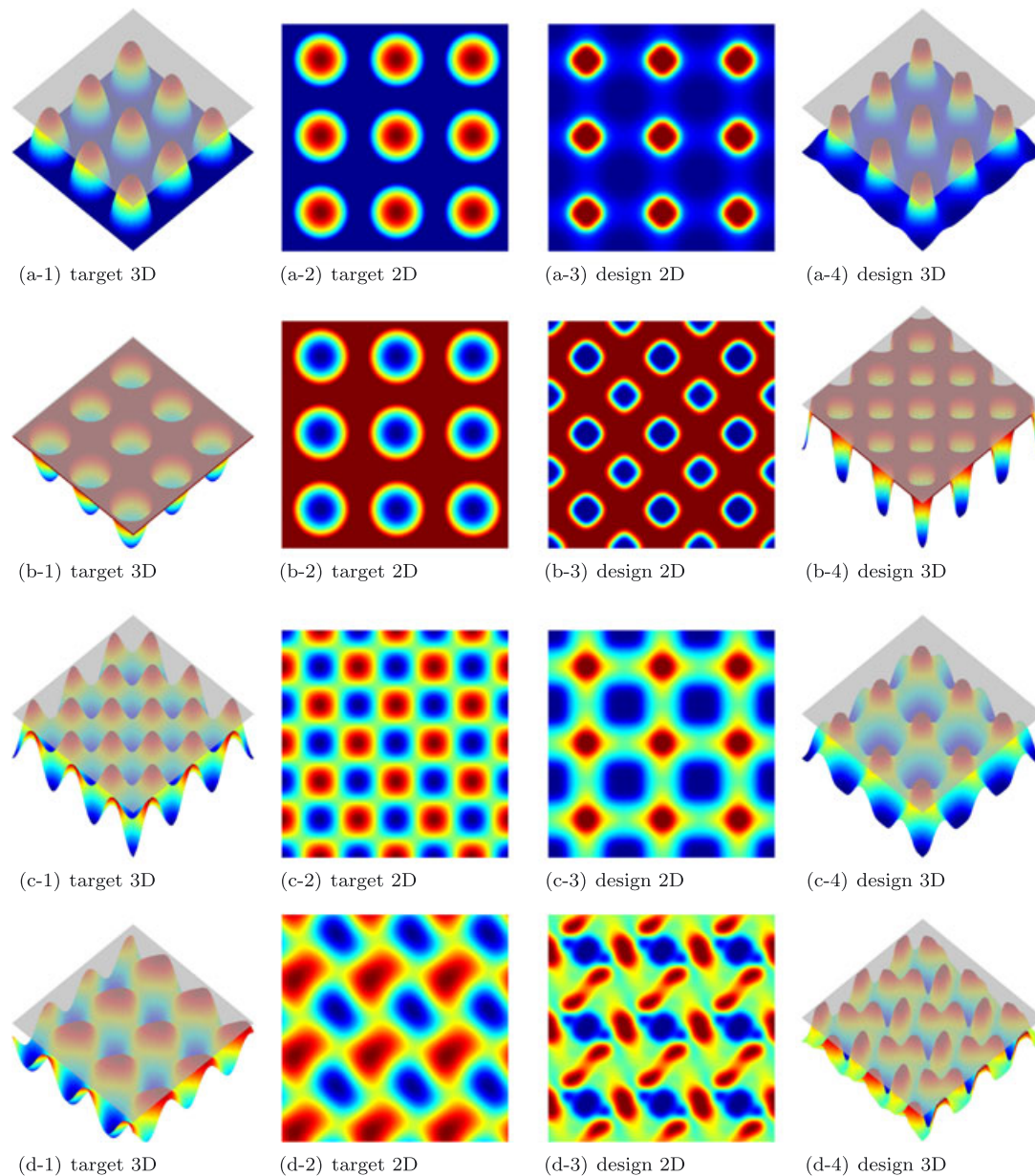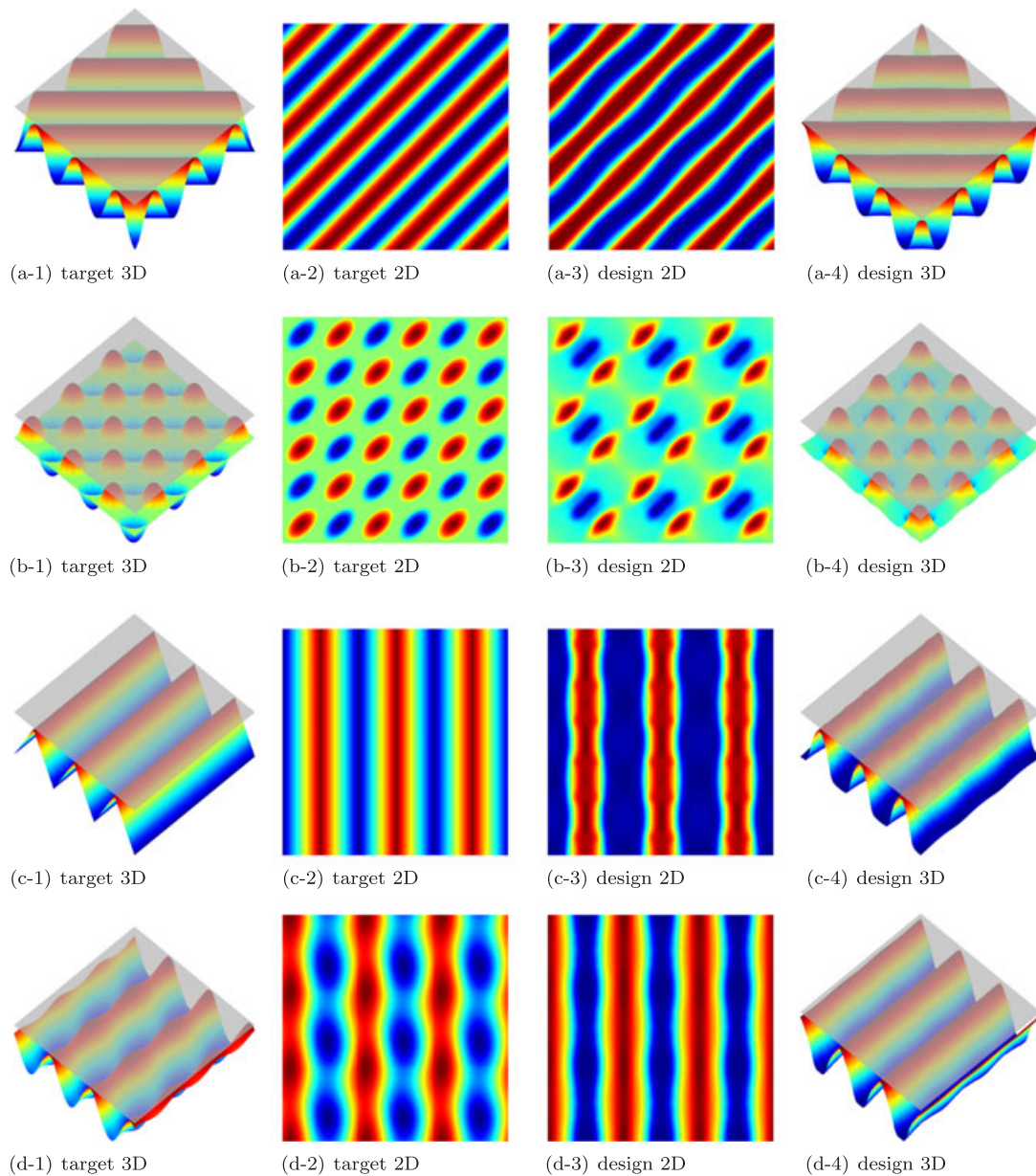
Figure 4. Benchmark target textures of the 0-OR-1 type displaying a macroscopically *anisotropic* response are depicted together with the output designs from the optimization algorithm based on the default numerical choices. The number of iterations to convergence were (a) 8 for the diagonal groove texture, (b) 75 for the ellipsoidal texture with alternating pillars and holes, (c) 21 for the trapezoidal pillar texture, and (d) 216 for the trapezoidal hole texture. See Table A.2 in Appendix B for corresponding target responses.

coordinates $(N/2, N/2)$ to $1 - s_0$ (unless s_0 is exactly equal to 0.5 in which case the perturbation is chosen as $1 - s_0 + \delta$ where δ is a small number). At convergence, the output set $\{A, C, \langle h \rangle\}$ will capture the input set $\{A^*, C^*, h_0\}$ to within the prescribed tolerances. However, because of the well-known non-uniqueness in microstructure design that is already particularly apparent in 0-TO-1 type textures with a macroscopically isotropic response (Figure 5), the topography of the designed texture depends on a number of parameters, including the initial s-distribution. Hence, the deciding factor for a suitable initial guess is the number of iterations to convergence and the visual quality of the design. Figure 7 summarizes a comparison between various initial guesses. Clearly, a uniform film distribution is undesirable as an initial guess because convergence is significantly delayed.

(a-1) target 3D   (a-2) target 2D   (a-3) design 2D   (a-4) design 3D

(b-1) target 3D   (b-2) target 2D   (b-3) design 2D   (b-4) design 3D

(c-1) target 3D   (c-2) target 2D   (c-3) design 2D   (c-4) design 3D

(d-1) target 3D   (d-2) target 2D   (d-3) design 2D   (d-4) design 3D

Figure 5. Benchmark target textures of the 0-TO-1 type displaying a macroscopically *isotropic* response are depicted together with the output designs from the optimization algorithm based on the default numerical choices. The number of iterations to convergence were (a) 78 for the circular bump texture, (b) 41 for the circular dimple texture, (c) 76 for the sinusoidal texture, and (d) 127 for the distorted sinusoidal texture. See Table A.3 in Appendix B for corresponding target responses. Note that the last texture is only weakly anisotropic and hence included in this list.

On the other hand, random inputs tend to deliver designs that can deviate significantly from the class of input textures chosen in this work. The default choice converges comparatively faster to a topography that closely reproduces the input texture.

5.3. Filtering radius and element type

For 0-OR-1 design, the default $Q1S1$ element not only prevents potential checkerboard patterns that often occur with the $Q1S0$ element in the absence of filtering [28, 64, 70, 71] but also delivers results that are of higher quality in relation to the target textures when filtering is employed. This is

Figure 6. Benchmark target textures of the 0-TO-1 type displaying a macroscopically *anisotropic* response are depicted together with the output designs from the optimization algorithm based on the default numerical choices. The number of iterations to convergence were (a) 15 for the diagonal wave texture, (b) 115 for the ellipsoidal texture with alternating bumps and dimples, (c) 29 for the triangular groove texture, and (d) 41 for the wavy groove texture. See Table A.4 in Appendix B for corresponding target responses.

summarized in Figure 8, where it is observed that the central feature is captured rather accurately, although areas with intermediate values of s remain. Moreover, the design with a $Q1S1$ element is relatively insensitive to the filter radius for the range of values tested. For 0-TO-1 design, $Q1S1$ element again prevents checkerboard patterns, although the texture quality of the $Q1S0$ element is comparable with the $Q1S1$ output once a suitable filter radius is selected (Figure 9). For a 0-TO-1 design, filtering strongly influences the texture for both element types due to linear filtering, with a clearly observable increase in the feature size with increasing filter radius.

To validate the analytical sensitivity expressions derived in Section 3, they are compared with their numerical counterparts in Appendix C based on the examples discussed in this section.

(a-1) default   (a-2) uniform   (a-3) 1st random   (a-4) 2nd random

(b-1) default   (b-2) uniform   (b-3) 1st random   (b-4) 2nd random
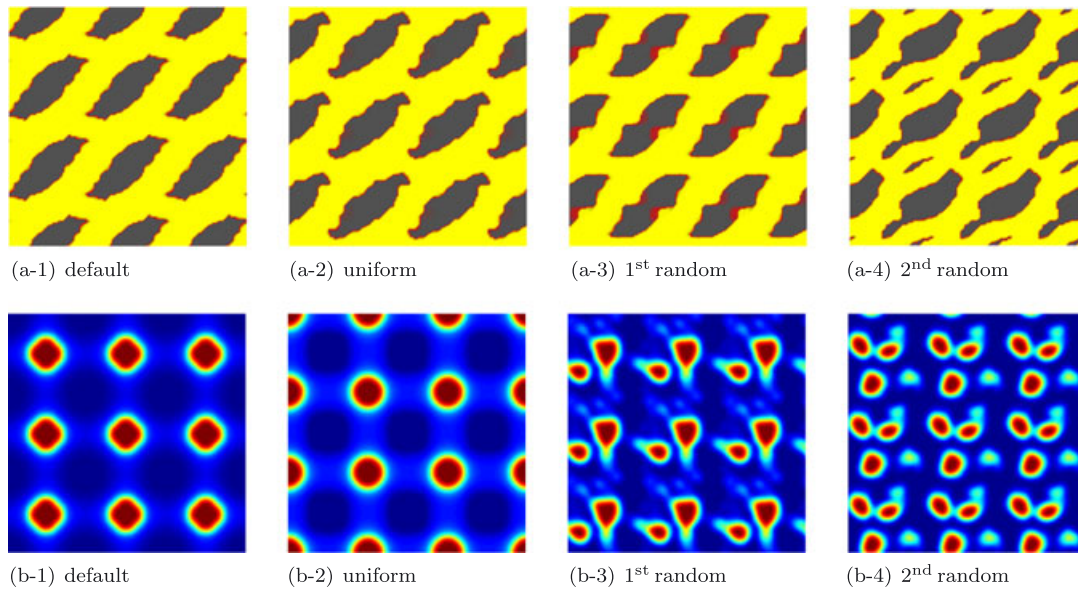
Figure 7. Influence of the initial guess is demonstrated using (a) 0-OR-1 type trapezoidal hole texture from Figure 4 and (b) 0-TO-1 type circular bump texture from Figure 5. The uniform guess employs a constant $s = s_0$ such that $h = h_0$, while the default guess additionally perturbs a degree of freedom. The two random guesses were generated from a Gaussian random number generator. The number of iterations to convergence were (a) {216, 529, 310, 1087} and (b) {78, 959, 103, 93}.

(a-1) no filter (Q1S0)   (a-2) $R = 1$ (Q1S0)   (a-3) $R = 2$ (Q1S0)   (a-4) $R = 4$ (Q1S0)   (a-5) $R = 8$ (Q1S0)

(b-1) no filter (Q1S1)   (b-2) $R = 1$ (Q1S1)   (b-3) $R = 2$ (Q1S1)   (b-4) $R = 4$ (Q1S1)   (b-5) $R = 8$ (Q1S1)
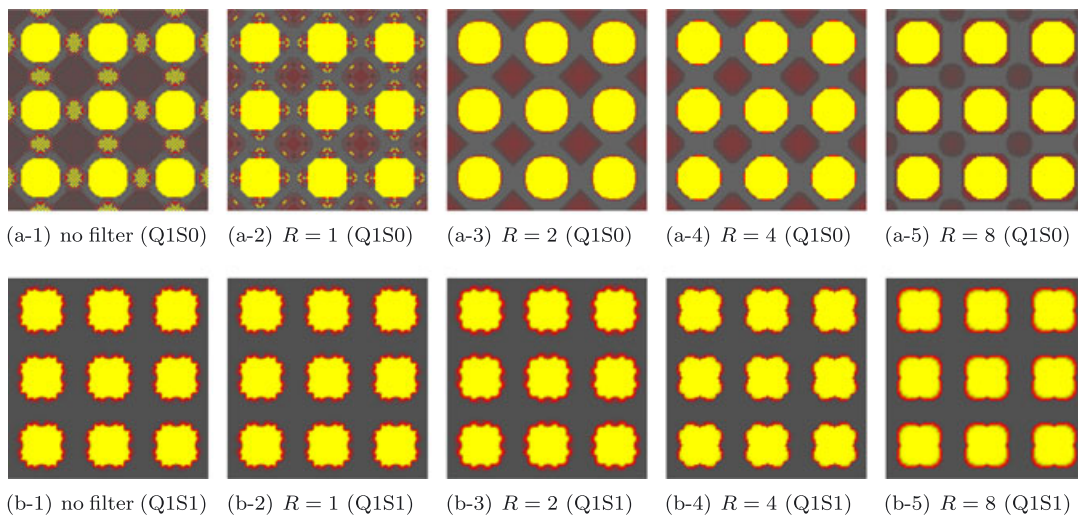
Figure 8. The effect of the element type (default: $Q1S1$) and filtering (default: $R = 4$) is demonstrated for 0-OR-1 type circular pillar texture from Figure 3 for (a) $Q1S0$ and (b) $Q1S1$ elements. The number of iterations to convergence were (a) {148, 125, 122, 145, 159} and (b) {110, 110, 93, 93, 229}.

5.4. Onsager's principle

For all the benchmark textures considered, A and C were symmetric tensors, except for the weakly non-symmetric C in the last 0-TO-1 textures of Figures 5 and 6 (Appendix B). The tensor A is necessarily symmetric and positive-definite [72]. As such, A obeys Onsager's principle but there is no such restriction for C, similar for instance to the tensors that characterize the Seebeck and Peltier effects in thermoelectricity [73]. This indicates that textures with significantly non-symmetric C tensors may be designed. In order to investigate this possibility, the optimization algorithm was applied to achieve a target C^* for a given h_0 without any restriction on A, which was formulated

(a-1) no filter (Q1S0)   (a-2) $R = 1$ (Q1S0)   (a-3) $R = 2$ (Q1S0)   (a-4) $R = 4$ (Q1S0)   (a-5) $R = 8$ (Q1S0)

(b-1) no filter (Q1S1)   (b-2) $R = 1$ (Q1S1)   (b-3) $R = 2$ (Q1S1)   (b-4) $R = 4$ (Q1S1)   (b-5) $R = 8$ (Q1S1)
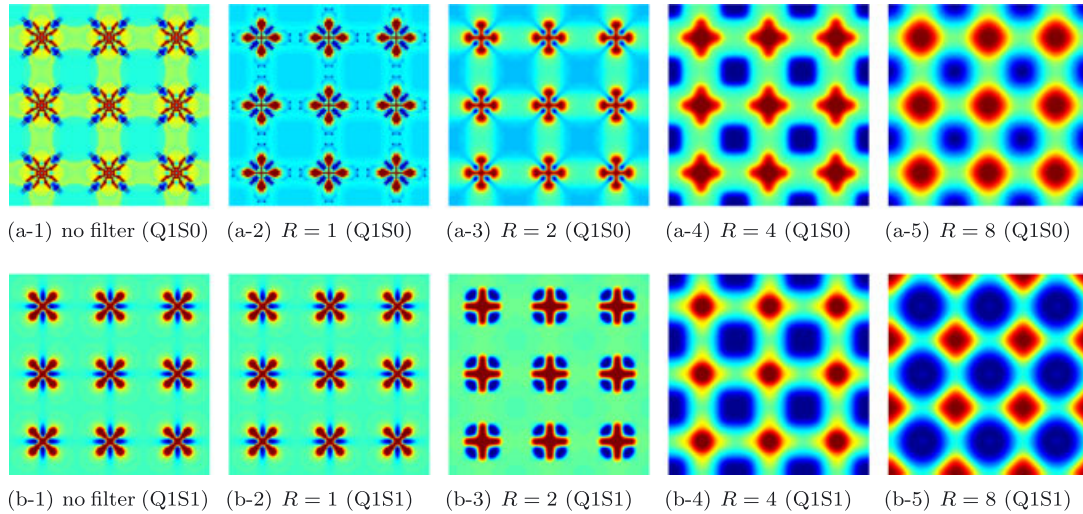
Figure 9. The effect of the element type (default: $Q1S1$) and filtering (default: $R = 4$) is demonstrated for 0-TO-1 type sinusoidal texture from Figure 5 for (a) $Q1S0$ and (b) $Q1S1$ elements. The number of iterations to convergence were (a) $\{80, 103, 85, 73, 107\}$ and (b) $\{79, 79, 144, 76, 116\}$.

(a-1) 0-OR-1: 2D   (a-2) 3D   (b-1) 0-TO-1: 2D   (b-2) 3D
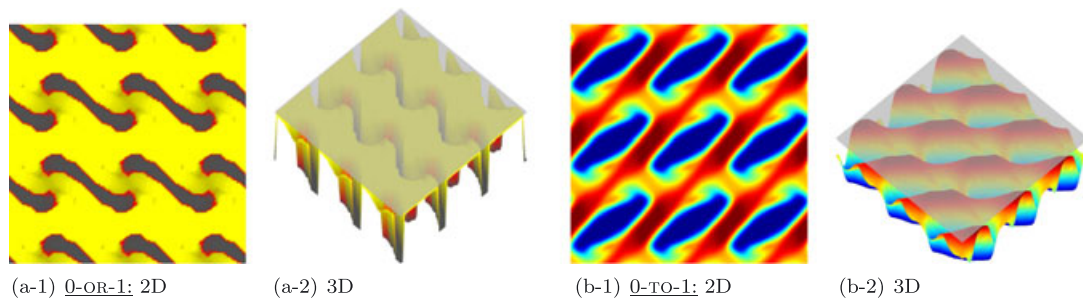
Figure 10. Textures designed according to the discussion in Section 5.4 in order to achieve significantly non-symmetric C values for (a) 0-OR-1 type design and (b) 0-TO-1 type design (see Table A.5 in Appendix B for corresponding macroscopic responses). The number of iterations to convergence were (a) 229 and (b) 44.

by removing the first contribution to φ in (4.7). For a 0-OR-1 example, h_0 was prescribed closer to h^- than h^+, which is expected to lead to holes on the surface rather than pillars. For a 0-TO-1 example, a mediocre h_0 value was prescribed, which is expected to lead to a smoothly varying texture. For both cases, the target C^* must be commensurate with the choice of h_0 because the addition of roughness to the stationary lower surface leads to a reduction of C with respect to the response of the homogeneous interface (Appendix B). Appropriate sample input values, found by trial and error, are (in μm):

$$
\begin{aligned}
\underline{0\text{-}\mathrm{OR}\text{-}1:} \quad h_0 = 0.80 \quad , \quad [\,C^*\,] = \begin{bmatrix} 0.05 & 0.00 \\ 0.10 & 0.10 \end{bmatrix} \quad , \\
\underline{0\text{-}\mathrm{TO}\text{-}1:} \quad h_0 = 1.45 \quad , \quad [\,C^*\,] = \begin{bmatrix} 0.40 & 0.10 \\ 0.20 & 0.30 \end{bmatrix} \quad .
\end{aligned}
\tag{4.10}
$$

The corresponding designs are depicted in Figure 10, which verify the previous assertion regarding the existence of such textures.

6. CONCLUSION

Surface texture can significantly impact the tribological performance of the interface and there-fore constitutes a tool with which the macroscopic interface response may be tuned. In this work,

a homogenization-based surface texture design framework has been presented in the context of hydrodynamic lubrication. Specifically, the goal was to obtain microscopic surface textures in order to achieve prescribed macroscopic interface tensors that appear in the homogenized Reynolds equation. For this purpose, a discrete design space was introduced, which employs either an element-wise constant design variable or a discretization of this variable using linear elements. The surface texture was subsequently indirectly described by formulating the film thickness in terms of the design variable after an intermediate filtering stage. Finally, the optimization problem was solved through the method of moving asymptotes, for which a sensitivity analysis of the macroscopic response of the texture was additionally carried out. Numerical investigations have demonstrated the ability of the framework to deliver both sharp (0-OR-1) textures as well as smoothly varying (0-TO-1) ones.

The presented homogenization-based microscopic design framework may be embedded within a two-scale setting in order to achieve a macroscopic goal, such as obtaining a desired pressure distribution or adjusting the dissipative effects over a lubrication domain, which may be further generalized toward the concurrent topology optimization of the macroscopic interface together with the microscopic one as in similar contexts for structures [57, 74–78]. In such settings, one would like to endow a surface, partially or fully, with a single texture or one would attempt to obtain a texture distribution with continuously varying statistical properties, for example, with an increasing root mean square roughness. Here, the macroscopic goal and the design constraints need to be carefully chosen because a homogenization-based analysis shows that in certain scenarios the optimal solution is no texture at all [79, 80]. Contrary to conventional texture optimization schemes based on a predetermined texture geometry, such as circular pillars or dimples, the present framework will naturally be equipped with the ability to capture the optimal pattern, which may span arbitrary 0-OR-1 and 0-TO-1 designs across the interface. The determination of such optimal design patterns in the case of a bilateral texture will additionally require extending the presented framework to the unsteady lubrication regime in order to address the oscillations in the macroscopic response. Such investigations will lead to a better understanding of the role of the texture in tuning interface lubrication and can benefit from as well as complement ongoing efforts in similar two-scale design problems involving microstructured materials.

APPENDIX A: UNILATERAL ROUGHNESS CASES

The purpose of this section is to elucidate the discussion of Section 2.3 regarding the four cases in Figure 1. CASE 1 and CASE 2 not only share the same $h = h_0 - \overline{h}$ distributions and, hence, the same $A = \overline{A}$ but also the same $h^+ + h^- = h^- = \overline{h}$ distribution, and hence, the same $B = \overline{B}$ by (2.14). However, for CASE 1 $V = \overline{U}$ so $C = h_0/2\,I + \overline{B}$, while for CASE 2 $V = -\overline{U}$ so $C = h_0/2\,I - \overline{B}$. In other words, the choice of the moving surface preserves B but changes a sign within C. A similar discussion holds between CASE 3 and CASE 4. To establish the link between CASE 1 and CASE 3, note that both share the same $V = \overline{U}$ and the same $h_0 = h_0 - \overline{h}$ distribution but the latter has $h^+ + h^- = h^+ = -\overline{h}$. Hence, the solution of the Ω-problem for CASE 3 will be the negative of that for CASE 1, leading to $B = -\overline{B}$ and therefore to $C = h_0/2\,I - \overline{B}$. In other words, the choice of the rough surface changes the sign of B as well as the sign within C.

In order to address the bilateral motion of the surfaces, let the lower surface in CASE 1 of Figure 1 be assigned a velocity U^- and the upper surface a velocity $U^+ = U^- + \overline{U}$, leading to $U = 2U^- + \overline{U}$ and $V = \overline{U}$. Then, directly via (2.4), one obtains $b = h_0 U^- + (h_0/2\,I + B)\overline{U}$ so that $b - h_0 U^-$, which represents the Couette contribution excluding the rigid translation of the interface fluid, is expressible in the form $C\overline{U}$. The discussion of the remaining cases is similar.

APPENDIX B: TARGET TEXTURE RESPONSE

The macroscopic responses associated with the textures in the numerical investigations of Section 5 are summarized in the succeeding text. The units are μm for $\{h_0, C\}$ and μm^3/Pa·s for A. In order to additionally assess the influence of the texture, the macroscopic response of the homogeneous interface with $h = h_0$ is also reported via the quantities

$$[A_0] = \begin{bmatrix} \frac{h_0^3}{12\mu} & 0 \\ 0 & \frac{h_0^3}{12\mu} \end{bmatrix} \quad , \quad [C_0] = \begin{bmatrix} \frac{h_0}{2} & 0 \\ 0 & \frac{h_0}{2} \end{bmatrix} \quad . \tag{A.1}$$

Note that, depending on the particular texture, the magnitude of A^* may be larger or smaller with respect to A_0, indicating that the texture can facilitate or hinder macroscopic fluid flux due to
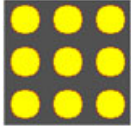
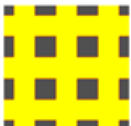Table A.1. Benchmark 0-OR-1 textures with a macroscopically *isotropic* response (Figure 3).

Target texture	Gap h_0	Homogeneous interface $[A_0]$	$[C_0]$	Heterogeneous interface $[A^*]$	$[C^*]$
	1.970	$\begin{bmatrix} 4.551 & 0 \\ 0 & 4.551 \end{bmatrix}$	$\begin{bmatrix} 0.985 & 0 \\ 0 & 0.985 \end{bmatrix}$	$\begin{bmatrix} 6.825 & 0 \\ 0 & 6.825 \end{bmatrix}$	$\begin{bmatrix} 0.680 & 0 \\ 0 & 0.680 \end{bmatrix}$
	1.130	$\begin{bmatrix} 0.859 & 0 \\ 0 & 0.859 \end{bmatrix}$	$\begin{bmatrix} 0.565 & 0 \\ 0 & 0.565 \end{bmatrix}$	$\begin{bmatrix} 0.0014 & 0 \\ 0 & 0.0014 \end{bmatrix}$	$\begin{bmatrix} 0.0545 & 0 \\ 0 & 0.0545 \end{bmatrix}$
	2.239	$\begin{bmatrix} 6.683 & 0 \\ 0 & 6.683 \end{bmatrix}$	$\begin{bmatrix} 1.120 & 0 \\ 0 & 1.120 \end{bmatrix}$	$\begin{bmatrix} 8.898 & 0 \\ 0 & 8.898 \end{bmatrix}$	$\begin{bmatrix} 0.866 & 0 \\ 0 & 0.866 \end{bmatrix}$
	0.861	$\begin{bmatrix} 0.380 & 0 \\ 0 & 0.380 \end{bmatrix}$	$\begin{bmatrix} 0.430 & 0 \\ 0 & 0.430 \end{bmatrix}$	$\begin{bmatrix} 0.0011 & 0 \\ 0 & 0.0011 \end{bmatrix}$	$\begin{bmatrix} 0.054 & 0 \\ 0 & 0.054 \end{bmatrix}$

Table A.2. Benchmark 0-OR-1 textures with a macroscopically *anisotropic* response (Figure 4).
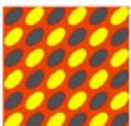
Target texture	Gap h_0	Homogeneous interface $[A_0]$	$[C_0]$	Heterogeneous interface $[A^*]$	$[C^*]$
	1.515	$\begin{bmatrix} 2.068 & 0 \\ 0 & 2.068 \end{bmatrix}$	$\begin{bmatrix} 0.757 & 0 \\ 0 & 0.757 \end{bmatrix}$	$\begin{bmatrix} 3.625 & 3.624 \\ 3.624 & 3.625 \end{bmatrix}$	$\begin{bmatrix} 0.39 & 0.33 \\ 0.33 & 0.39 \end{bmatrix}$
	1.550	$\begin{bmatrix} 2.217 & 0 \\ 0 & 2.217 \end{bmatrix}$	$\begin{bmatrix} 0.775 & 0 \\ 0 & 0.775 \end{bmatrix}$	$\begin{bmatrix} 1.949 & 0.863 \\ 0.863 & 1.949 \end{bmatrix}$	$\begin{bmatrix} 0.446 & 0.132 \\ 0.132 & 0.446 \end{bmatrix}$
	2.062	$\begin{bmatrix} 5.215 & 0 \\ 0 & 5.215 \end{bmatrix}$	$\begin{bmatrix} 1.031 & 0 \\ 0 & 1.031 \end{bmatrix}$	$\begin{bmatrix} 5.322 & 3.338 \\ 3.338 & 7.031 \end{bmatrix}$	$\begin{bmatrix} 0.546 & 0.306 \\ 0.307 & 0.702 \end{bmatrix}$
	1.038	$\begin{bmatrix} 0.667 & 0 \\ 0 & 0.667 \end{bmatrix}$	$\begin{bmatrix} 0.520 & 0 \\ 0 & 0.520 \end{bmatrix}$	$\begin{bmatrix} 0.0020 & 0.0013 \\ 0.0013 & 0.0027 \end{bmatrix}$	$\begin{bmatrix} 0.0553 & -0.0007 \\ -0.0007 & 0.0541 \end{bmatrix}$

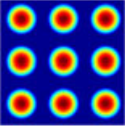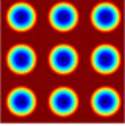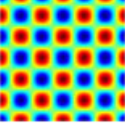Table A.3. Benchmark 0-TO-1 textures with a macroscopically *isotropic* response (Figure 5).
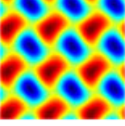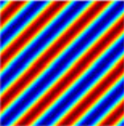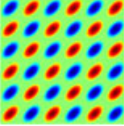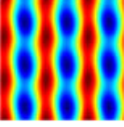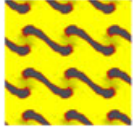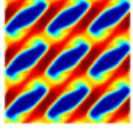
Target texture	Gap h_0	Homogeneous interface $[A_0]$	$[C_0]$	Heterogeneous interface $[A^*]$	$[C^*]$
	2.359	$\begin{bmatrix} 7.817 & 0 \\ 0 & 7.817 \end{bmatrix}$	$\begin{bmatrix} 1.180 & 0 \\ 0 & 1.180 \end{bmatrix}$	$\begin{bmatrix} 8.077 & 0 \\ 0 & 8.077 \end{bmatrix}$	$\begin{bmatrix} 0.955 & 0 \\ 0 & 0.955 \end{bmatrix}$
	0.741	$\begin{bmatrix} 0.242 & 0 \\ 0 & 0.242 \end{bmatrix}$	$\begin{bmatrix} 0.370 & 0 \\ 0 & 0.370 \end{bmatrix}$	$\begin{bmatrix} 0.0017 & 0 \\ 0 & 0.0017 \end{bmatrix}$	$\begin{bmatrix} 0.0512 & 0 \\ 0 & 0.0512 \end{bmatrix}$
	1.550	$\begin{bmatrix} 2.217 & 0 \\ 0 & 2.217 \end{bmatrix}$	$\begin{bmatrix} 0.775 & 0 \\ 0 & 0.775 \end{bmatrix}$	$\begin{bmatrix} 1.852 & 0 \\ 0 & 1.852 \end{bmatrix}$	$\begin{bmatrix} 0.558 & 0 \\ 0 & 0.558 \end{bmatrix}$
	1.411	$\begin{bmatrix} 1.673 & 0 \\ 0 & 1.673 \end{bmatrix}$	$\begin{bmatrix} 0.706 & 0 \\ 0 & 0.706 \end{bmatrix}$	$\begin{bmatrix} 1.301 & 0.041 \\ 0.041 & 1.220 \end{bmatrix}$	$\begin{bmatrix} 0.469 & 0.034 \\ 0.036 & 0.458 \end{bmatrix}$

Table A.4. Benchmark 0-TO-1 textures with a macroscopically *anisotropic* response (Figure 6).

Target texture	Gap h_0	Homogeneous interface $[A_0]$	$[C_0]$	Heterogeneous interface $[A^*]$	$[C^*]$
	1.550	$\begin{bmatrix} 2.217 & 0 \\ 0 & 2.217 \end{bmatrix}$	$\begin{bmatrix} 0.775 & 0 \\ 0 & 0.775 \end{bmatrix}$	$\begin{bmatrix} 2.554 & 2.544 \\ 2.544 & 2.554 \end{bmatrix}$	$\begin{bmatrix} 0.423 & 0.352 \\ 0.352 & 0.423 \end{bmatrix}$
	1.550	$\begin{bmatrix} 2.217 & 0 \\ 0 & 2.217 \end{bmatrix}$	$\begin{bmatrix} 0.775 & 0 \\ 0 & 0.775 \end{bmatrix}$	$\begin{bmatrix} 1.981 & 0.389 \\ 0.389 & 1.981 \end{bmatrix}$	$\begin{bmatrix} 0.620 & 0.068 \\ 0.068 & 0.620 \end{bmatrix}$
	1.585	$\begin{bmatrix} 2.372 & 0 \\ 0 & 2.372 \end{bmatrix}$	$\begin{bmatrix} 0.793 & 0 \\ 0 & 0.793 \end{bmatrix}$	$\begin{bmatrix} 4.156 & 0 \\ 0 & 0.055 \end{bmatrix}$	$\begin{bmatrix} 0.775 & 0 \\ 0 & 0.122 \end{bmatrix}$
	1.488	$\begin{bmatrix} 1.959 & 0 \\ 0 & 1.959 \end{bmatrix}$	$\begin{bmatrix} 0.744 & 0 \\ 0 & 0.744 \end{bmatrix}$	$\begin{bmatrix} 3.649 & 0.002 \\ 0.002 & 0.176 \end{bmatrix}$	$\begin{bmatrix} 0.728 & 0.0042 \\ 0.0023 & 0.210 \end{bmatrix}$

a pressure gradient. On the other hand, the magnitude of C^* is always less than the magnitude of C_0. This is due to the fact that, in the specialized setup of CASE 1 that is representative of alternate scenarios (Appendix A), the stationary rough surface holds fluid back from being dragged along with the moving upper surface, that is, $\overline{B}$ has predominantly negative entries.

Table A.5. Textures designed according to the discussion in Section 5.4 (Figure 10).

Texture	Gap h_0	Homogeneous interface $[A_0]$	$[C_0]$	Heterogeneous interface $[A]$	$[C]$
	0.800	$\begin{bmatrix} 0.305 & 0 \\ 0 & 0.305 \end{bmatrix}$	$\begin{bmatrix} 0.400 & 0 \\ 0 & 0.400 \end{bmatrix}$	$\begin{bmatrix} 0.0015 & -0.001 \\ -0.001 & 0.289 \end{bmatrix}$	$\begin{bmatrix} 0.054 & 0 \\ 0.095 & 0.101 \end{bmatrix}$
	1.450	$\begin{bmatrix} 1.815 & 0 \\ 0 & 1.815 \end{bmatrix}$	$\begin{bmatrix} 0.725 & 0 \\ 0 & 0.725 \end{bmatrix}$	$\begin{bmatrix} 1.043 & 0.782 \\ 0.782 & 0.853 \end{bmatrix}$	$\begin{bmatrix} 0.397 & 0.116 \\ 0.182 & 0.304 \end{bmatrix}$

(a-1) $Q1S0$: analytical (a-2) $Q1S1$: analytical (a-3) $Q1S0$: analytical (a-4) $Q1S1$: analytical

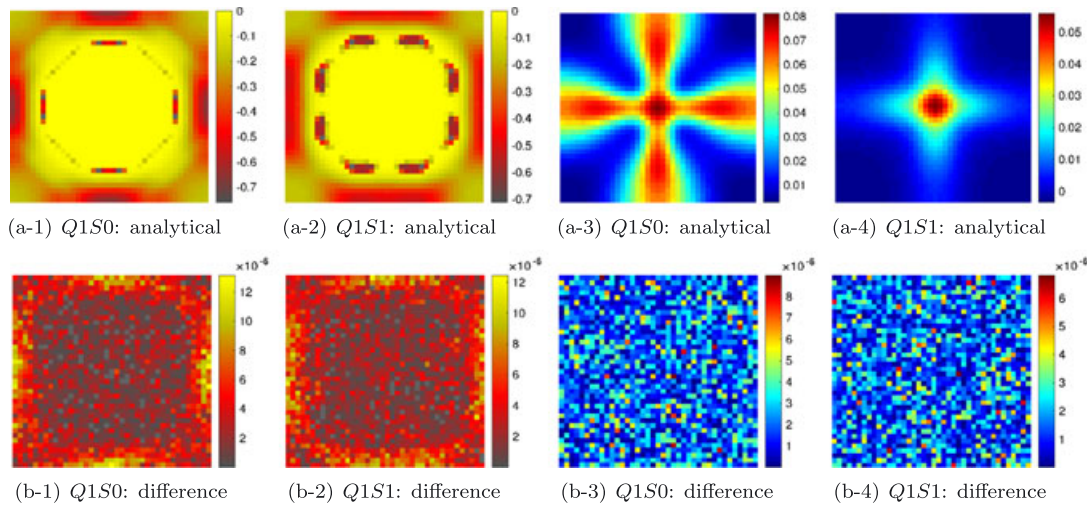(b-1) $Q1S0$: difference (b-2) $Q1S1$: difference (b-3) $Q1S0$: difference (b-4) $Q1S1$: difference

Figure A.1. The analytical (A) sensitivity distributions are provided and compared with the numerical (N) sensitivities through the difference $\left| (\partial\varphi/\partial s^I)_A - (\partial\varphi/\partial s^I)_N \right|$ on converged 0-OR-1 and 0-TO-1 type textures from figures 8 and 9 for both $Q1S0$ and $Q1S1$ elements ($R = 4$).

APPENDIX C: SENSITIVITY VALIDATION

The analytical sensitivity expressions, derived in Section 3 and employed throughout the numerical investigations, will be compared with their numerical counterparts for validation. For this purpose, the 0-OR-1 and 0-TO-1 type designs considered in Figures 8 and 9 with $Q1S0$ and $Q1S1$ elements will be employed at the default filter radius. The comparison is carried out based on the sensitivity $\partial\varphi/\partial s^I$ of the objective function (4.7) at the converged textures, that is, at the last optimization iteration. The numerical sensitivity is computed via second-order finite difference by sequentially perturbing each s^I value through 10^{-4}. The results in Figure A.1 demonstrate the agreement between the analytical and numerical sensitivities.

ACKNOWLEDGEMENTS

REFERENCES

1. Bendsøe MP, Sigmund O. *Topology Optimization: Theory, Methods and Applications* (2nd edition). Springer: Berlin, Heidelberg, New York, 2004.
2. Christensen PW, Klarbring A. *An Introduction to Structural Optimization*. Springer: Berlin, Heidelberg, New York, 2010.
3. Allaire G, Jouve F, Toader AM. Structural optimization using sensitivity analysis and a level-set method. *Journal of Computational Physics* 2004; **194**(1):363–393.
4. Pedro HTC, Kobayashi MH. On a cellular division method for topology optimization. *International Journal for Numerical Methods in Engineering* 2011; **88**(11):1175–1197.
5. Wallin M, Ivarsson N, Ristinmaa M. Large strain phase-field-based multi-material topology optimization. *International Journal for Numerical Methods in Engineering* 2015; **104**(9):887–904.
6. Park J, Sutradhar A. A multi-resolution method for 3d multi-material topology optimization. *Computer Methods in Applied Mechanics and Engineering* 2015; **285**:571–586.
7. Lee JS, Göransson P, Kim YY. Topology optimization for three-phase materials distribution in a dissipative expansion chamber by unified multiphase modeling approach. *Computer Methods in Applied Mechanics and Engineering* 2015; **287**:191–211.
8. Gao T, Zhang W. A mass constraint formulation for structural topology optimization with multiphase materials. *International Journal for Numerical Methods in Engineering* 2011; **88**(8):774–796.
9. Swan CC, Kosaka I. Voigt-Reuss topology optimization for structures with linear elastic material behaviours. *International Journal for Numerical Methods in Engineering* 1997; **40**(16):3033–3057.
10. Nakshatrala P, Tortorelli D. Topology optimization for effective energy propagation in rate-independent elastoplastic material systems. *Computer Methods in Applied Mechanics and Engineering* 2015; **295**:305–326.
11. Evgrafov A, Maute K, Yang RG, Dunn ML. Topology optimization for nano-scale heat transfer. *International Journal for Numerical Methods in Engineering* 2009; **77**(2):285–300.
12. Takezawa A, Kitamura M. Topology optimization of compliant circular path mechanisms based on an aggregated linear system and singular value decomposition. *International Journal for Numerical Methods in Engineering* 2012; **89**(6):706–725.
13. Carbonari RC, Silva ECN, Paulino GH. Multi-actuated functionally graded piezoelectric micro-tools design: a multiphysics topology optimization approach. *International Journal for Numerical Methods in Engineering* 2009; **77**(3):301–336.
14. Kiyono C, Silva E, Reddy J. Design of laminated piezocomposite shell transducers with arbitrary fiber orientation using topology optimization approach. *International Journal for Numerical Methods in Engineering* 2012; **90**(12):1452–1484.
15. Clausen A, Aage N, Sigmund O. Topology optimization of coated structures and material interface problems. *Computer Methods in Applied Mechanics and Engineering* 2015; **290**:524–541.
16. Boucard PA, Buytet S, Guidault PA. A multiscale strategy for structural optimization. *International Journal for Numerical Methods in Engineering* 2009; **78**(1):101–126.
17. Chen WH, Ou CR. Shape optimization in contact problems with desired contact traction distribution on the specified contact surface. *Computational Mechanics* 1995; **15**(6):534–545.
18. Lee JH, Singer JP, Thomas EL. Micro-/nanostructured mechanical metamaterials. *Adv. Mater.* 2012; **24**:4782–4810.
19. Guest JK. Optimizing the layout of discrete objects in structures and materials: A projection-based topology optimization approach. *Computer Methods in Applied Mechanics and Engineering* 2015; **283**:330–351.
20. Huang X, Zhou S, Sun G, Li G, Xie YM. Topology optimization for microstructures of viscoelastic composite materials. *Computer Methods in Applied Mechanics and Engineering* 2015; **283**:503–516.
21. Fujii D, Chen B C, Kikuchi N. Composite material design of two-dimensional structures using the homogenization design method. *International Journal for Numerical Methods in Engineering* 2001; **50**(9):2031–2051.
22. Zhang W, Sun S. Scale-related topology optimization of cellular materials and structures. *International Journal for Numerical Methods in Engineering* 2006; **68**(9):993–1011.
23. Zohdi TI. Constrained inverse formulations in random material design. *Computer Methods in Applied Mechanics and Engineering* 2003; **192**:3179–3194.
24. Torquato S. *Random Heterogeneous Materials: Microstructure and Macroscopic Properties*. Springer: Berlin Heidelberg New York, 2002.
25. Feng JW, Cen S, Li CF, Owen DRJ. Statistical reconstruction and Karhunen-Loeve expansion for multiphase random media. *International Journal for Numerical Methods in Engineering* 2016; **105**(1):3–32.
26. Bendsøe MP, Kikuchi N. Generating optimal topologies in structural design using a homogenization method. *Computer Methods in Applied Mechanics and Engineering* 1988; **71**(2):197–224.
27. Bendsøe MP. Optimal shape design as a material distribution problem. *Structural Optimization* 1989; **1**(4):193–202.
28. Diaz A, Sigmund O. Checkerboard patterns in layout optimization. *Structural Optimization* 1995; **10**(1):40–45.
29. Bendsøe MP, Sigmund O. Material interpolation schemes in topology optimization. *Archive of Applied Mechanics* 1999; **69**(9-10):635–654.
30. Rayleigh L. Notes on the theory of lubrication. *Philosophical Magazine* 1918; **35**(205):1–12.
31. Maday CJ. A bounded variable approach to the optimum slider bearing. *Journal of Tribology* 1968; **90**(1):240–242.
32. Yoon SJ, Choi DH. Design optimization of the taper-flat slider positioned by a rotary actuator. *Journal of Tribology* 1995; **117**(4):588–593.
33. Zhu H, Bogy DB. Direct algorithm and its application to slider air-bearing surface optimization. *Magnetics, IEEE Transactions on* 2002; **38**(5):2168–2170.

34. Yoon SJ, Choi DH. Adjoint design sensitivity analysis of molecular gas film lubrication sliders. *Journal of Tribology* 2003; **125**(1):145–151.
35. Lu CJ, Wang TK. New designs of HDD air-lubricated sliders via topology optimization. *Journal of Tribology* 2004; **126**(1):171–176.
36. Zhu H, Bogy DB. Hard disc drive air bearing design: modified direct algorithm and its application to slider air bearing surface optimization. *Tribology International* 2004; **37**(2):193–201.
37. Yoon SJ, Choi DH. Topology designs of slider air bearings. *Journal of Tribology* 2004; **126**(2):342–346.
38. Zhang J, Talke FE. Optimization of slider air bearing contours using the combined genetic algorithm-subregion approach. *Tribology International* 2005; **38**(6):566–573.
39. Maday CJ. The maximum principle approach to the optimum one-dimensional journal bearing. *Journal of Tribology* 1970; **92**(3):482–487.
40. Zengeya M, Gadala M. Optimization of journal bearings using a hybrid scheme. *Proceedings of the Institution of Mechanical Engineers, Part J: Journal of Engineering Tribology* 2007; **221**(5):591–607.
41. Hashimoto H. Optimum design of high-speed, short journal bearings by mathematical programming. *Tribology Transactions* 1997; **40**(2):283–293.
42. Yang BS, Lee YH, Choi BK, Kim HJ. Optimum design of short journal bearings by artificial life algorithm. *Tribology International* 2001; **34**(7):427–435.
43. Hashimoto H, Matsumoto K. Improvement of operating characteristics of high-speed hydrodynamic journal bearings by optimum design: part I — formulation of methodology and its application to elliptical bearing design. *Journal of Tribology* 2001; **123**(2):305–312.
44. Hirani H, Suh NP. Journal bearing design using multiobjective genetic algorithm and axiomatic design approaches. *Tribology International* 2005; **38**(5):481–491.
45. Szeri AZ. *Fluid Film Lubrication*. Cambridge University Press: New York, 2011.
46. Hamrock B, Schmid S, Jacobson B. *Fundamentals of fluid film lubrication*. CRC Press: Boca Raton, 2004.
47. Buscaglia GC, Ausas RF, Jai M. Optimization tools in the analysis of micro-textured lubricated devices. *Inverse Problems in Science and Engineering* 2006; **14**:365–378.
48. Stachowiak G, Podsiadlo P. 3-D characterization, optimization, and classification of textured surfaces. *Tribology Letters* 2008; **32**(1):13–21.
49. Murthy AN, Duwensee M, Talke FE. Numerical simulation of the head/disk interface for patterned media. *Tribology Letters* 2010; **38**(1):47–55.
50. Dobrica MB, Fillon M, Pascovici MD, Cicone T. Optimizing surface texture for hydrodynamic lubricated contacts using a mass-conserving numerical approach. *Proceedings of the Institution of Mechanical Engineers, Part J: Journal of Engineering Tribology* 2010; **224**(8):737–750.
51. Fesanghary M, Khonsari MM. On the shape optimization of self-adaptive grooves. *Tribology Transactions* 2011; **54**(2):256–264.
52. Guzek A, Podsiadlo P, Stachowiak GW. Optimization of textured surface in 2D parallel bearings governed by the Reynolds equation including cavitation and temperature. *Tribology Online* 2013; **8**(1):7–21.
53. Scaraggi M. Optimal textures for increasing the load support in a thrust bearing pad geometry. *Tribology Letters* 2014; **53**(1):127–143.
54. Shen C, Khonsari MM. Numerical optimization of texture shape for parallel surfaces under unidirectional and bidirectional sliding. *Tribology International* 2015; **82**:1–11.
55. Sigmund O, Torquato S. Design of materials with extreme thermal expansion using a three-phase topology optimization method. *J. Mech. Phys. Solids* 1997; **45**:1037–1067.
56. Niu B, Yan J, Cheng G. Optimum structure with homogeneous optimum cellular material with maximum fundamental frequency. *Struct Multidisc Optim* 2009; **39**:115–132.
57. Kato J, Yachi D, Terada K, Kyoya T. Topology optimization of micro-structure for composites applying a decoupling multi-scale analysis. *Struct Multidisc Optim* 2014; **49**:595–608.
58. Yan X, Huang X, Zha Y, Xie YM. Concurrent topology optimization of structures and their composite microstructures. *Computers and Structures* 2014; **133**:103–110.
59. Clausen A, Wang F, Jensen JS, Sigmund O, Lewis JA. Topology optimized architectures with programmable Poisson's ratio over large deformations. *Adv. Mater.* 2015; **27**:5523–5527.
60. Bayada G, Chambat M. Homogenization of the Stokes system in a thin film flow with rapidly varying thickness. *Mathematical Modeling and Numerical Analysis* 1989; **23**:205–234.
61. Bayada G, Ciuperca I, Jai M. Homogenized elliptic equations and variational inequalities with oscillating parameters. application to the study of thin flow behavior with rough surfaces. *Nonlinear Analysis: Real World Applications* 2006; **7**:950–966.
62. Kabacaoğlu G, Temizer İ. Homogenization of soft interfaces in time-dependent hydrodynamic lubrication. *Computational Mechanics* 2015; **56**:421–441.
63. Buscaglia G, Jai M. Sensitivity analysis and Taylor expansions in numerical homogenization problems. *Numerische Mathematik* 2000; **85**:49–75.
64. Matsui K, Terada K. Continuous approximation of material distribution for topology optimization. *International Journal for Numerical Methods in Engineering* 2004; **59**:1925–1944.
65. Svanberg K, Svärd H. Density filters for topology optimization based on the Pythagorean means. *Struct Multidisc Optim* 2013; **48**:859–875.
66. Bourdin B. Filters in topology optimization. *International Journal for Numerical Methods in Engineering* 2001; **50**(9):2143–2158.

67. Sigmund O. Morphology-based black and white filters for topology optimization. *Struct Multidisc Optim* 2007; **33**:401–424.
68. Svanberg K. The method of moving asymptotes — a new method for structural optimization. *International Journal for Numerical Methods in Engineering* 1987; **24**:359–373.
69. The MMA routines (`mmasub.m` and `subsolv.m`) employed were provided by K Svanberg on 30.06.2014.
70. Sigmund O, Petersson J. Numerical instabilities in topology optimization: a survey on procedures dealing with checkerboards, mesh-dependencies and local minima. *Structural Optimization* 1998; **16**(1):68–75.
71. Zhou M, Shyy YK, Thomas HL. Checkerboard and minimum member size control in topology optimization. *Structural and Multidisciplinary Optimization* 2001; **21**(2):152–158.
72. Sanchez-Palencia E. *Non-Homogeneous Media and Vibration Theory*. Springer-Verlag: Berlin, Heidelberg, New York, 1980.
73. Newnham RE. *Properties of Materials: Anisotropy, Symmetry, Structure*. Oxford University Press: Oxford, 2005.
74. Nakshatrala P, Tortorelli D, Nakshatrala K. Nonlinear structural design using multiscale topology optimization. part i: Static formulation. *Computer Methods in Applied Mechanics and Engineering* 2013; **261-262**:167–176.
75. Xia L, Breitkopf P. Concurrent topology optimization design of material and structure within nonlinear multiscale analysis framework. *Computer Methods in Applied Mechanics and Engineering* 2014; **278**:524–542.
76. Xia L, Breitkopf P. Multiscale structural topology optimization with an approximate constitutive model for local material microstructure. *Computer Methods in Applied Mechanics and Engineering* 2015; **286**:147–167.
77. Chen BC, Silva ECN, Kikuchi N. Advances in computational design and optimization with application to mems. *International Journal for Numerical Methods in Engineering* 2001; **52**(1-2):23–62.
78. Alexandersen J, Lazarov BS. Topology optimisation of manufacturable microstructural details without length scale separation using a spectral coarse basis preconditioner. *Computer Methods in Applied Mechanics and Engineering* 2015; **290**:156–182.
79. Buscaglia GC, Ciuperca I, Jai M. The effect of periodic textures on the static characteristics of thrust bearings. *Journal of Tribology* 2005; **127**:899–902.
80. Buscaglia GC, Ciuperca I, Jai M. On the optimization of surface textures for lubricated contacts. *Journal of Mathematical Analysis and Applications* 2007; **335**:1309–1327.